Constraining an Eddy Energy Dissipation Rate due to Relative Wind Stress for use in Energy Budget-Based Eddy Parameterisations

Thomas Wilder[1,2], Xiaoming Zhai[1], David Munday[3], and Manoj Joshi[4]

[1]School of Environmental Sciences, University of East Anglia, Norwich, UK
[2]National Centre for Atmospheric Science, Department of Meteorology, University of Reading, Reading, UK.
[3]British Antarctic Survey, High Cross, Madingley Road, Cambridge, UK
[4]Climatic Research Unit, University of East Anglia, Norwich, UK

Correspondence: Thomas Wilder (t.m.wilder@reading.ac.uk)

Abstract. A geostrophic eddy energy dissipation rate due to the interaction of the large-scale wind field and mesoscale ocean currents, or *relative wind stress*, is derived here for use in eddy energy budget-based eddy parameterisations. We begin this work by analytically deriving a relative wind stress damping term and a baroclinic geostrophic eddy energy equation. The time evolution of this analytical eddy energy in response to relative wind stress damping is compared directly with a baroclinic eddy in a general circulation model for both anticyclones and cyclones. The dissipation of eddy energy is comparable between each model and eddy type, although the numerical model diverges from the analytical model at around day 150, likely due to the presence of nonlinear baroclinic processes. A constrained dissipation rate due to relative wind stress is then proposed using terms from the analytical eddy energy budget. This dissipation rate depends on the potential energy of the eddy thermocline displacement, which also depends on eddy length scale. Using an array of ocean datasets, and computing two forms for the eddy length scale, a range of values for the dissipation rate are presented. The analytical dissipation rate is found to vary from 0.25 to 4 times that of a constant dissipation rate employed in previous studies. The dissipation rates are generally enhanced in the Southern Ocean, but smaller in the western boundaries. This proposed dissipation rate offers a tool to parameterise the damping of total eddy energy in coarse resolution global climate models, and may have implications for a wide range of climate processes.

1   Introduction

Satellite altimetry data has revealed an ocean surface scattered with geostrophic eddies (Wunsch and Stammer, 1998). Eddies are highly energetic features, containing 80% of the ocean's kinetic energy, and also exhibit a wide swathe of spatial and temporal scales. They can be found most prominently in the western boundary currents (e.g. Gulf Stream) and Southern Ocean, and are generated primarily via baroclinic instability of the mean flow (Holland and Lin, 1975). In the global ocean, eddies regulate ocean heat uptake (Zhai and Greatbatch, 2006; Zhang and Vallis, 2013; Griffies et al., 2015), modulate volume transport (Holland, 1978; Hallberg and Gnanadesikan, 2006; Wang et al., 2017; Zhai and Yang, 2022), and influence the exchange of ocean properties between the surface and interior (McGillicuddy et al., 1998; Dove et al., 2022). Faithfully representing eddy

~~dynamics~~ eddying feedbacks onto the mean state in non-eddy resolving ocean models is therefore integral for accurate future climate projections.

25   The representation of mesoscale eddies in coarse resolution ocean models is usually carried out using the Gent-McWilliams (GM) parameterisation (Gent and McWilliams, 1990; Gent et al., 1995). The GM scheme ~~advects tracers downgradient~~represents mesoscale eddy mixing, mimicking the process of isopycnal flattening ~~by ocean eddies~~ and release of potential energy via baroclinic instability. As a result of the GM scheme in global ocean models, significant improvements have been made to the ocean circulation (Hirst and McDougall, 1996; Gordon et al., 2000). Danabasoglu et al. (1994) implemented the GM scheme in
30   a non-eddy resolving ocean model and found this produced a sharper thermocline and a reduced Southern Ocean meridional overturning. The scheme used by Danabasoglu et al. (1994) considered only a constant GM transfer coefficient, ~~κ~~κ_{gm}, although further studies have devised analytical and numerically inferred forms of ~~κ~~ κ_{gm} that depend on space and time (Treguier et al., 1997; Visbeck et al., 1997; Ferreira et al., 2005). However, the use of these GM transfer coefficients do not produce a realistic energetic flow field. This is because the GM scheme dissipates all of the potential energy released (Tandon and Garrett, 1996),
35   and as such ignores classical geostrophic turbulence theory (Charney, 1971).

    With all this in mind, a new fleet of GM style eddy parameterisations have been developed that aim to be more energetically consistent (Eden and Greatbatch, 2008; Marshall et al., 2012; Jansen et al., 2019; Bachman, 2019). Eddy energy budget-based eddy parameterisations define a GM transfer coefficient that varies in space and time through its dependence on total eddy energy E, or, eddy kinetic energy. One such parameterisation is called GEOMETRIC and was developed in Marshall
40   et al. (2012) and later implemented in ocean circulation models (Mak et al., 2018, 2022b). GEOMETRIC time steps a depth integrated eddy energy budget to inform the value of a transfer coefficient,

$$\kappa_{gm} = \alpha E \frac{N}{M^2} \tag{1}$$

where α is a tuning parameter, N is the vertical buoyancy frequency, and M is the horizontal buoyancy frequency. The κ_{gm} term forms part of the source term for eddy energy since potential energy is released from the mean flow to generate eddies.
45   Results from the implementation of GEOMETRIC present improvements to the large scale ocean circulation through the emergence of eddy saturation (Mak et al., 2017) and even eddy compensation (Mak et al., 2018).

    Whilst energy budget-based eddy parameterisations offer improvements, there are current uncertainties surrounding the dissipation rate of eddy energy, which will feed back into uncertainties in the GM coefficient. It was revealed by Marshall et al. (2017) through theory and a channel model that varying bottom drag could modify volume transport and ocean heat uptake. Later,
50   Mak et al. (2022b) investigated the impact of varying eddy energy dissipation timescales on the global ocean. They found that less damping of eddy energy led to a reduction in heat uptake, while increased damping led to the opposite effect. The authors attributed these differences in heat uptake to changes in the global pycnocline depth, as well as changes to the ~~ACC and AMOC transports~~volume transport of the Antarctic Circumpolar Current and Atlantic Meridional Overturning Cirulation (AMOC). It is therefore necessary to try and constrain an eddy energy dissipation rate to obtain a realistic projection of the global climate.
55   However, the dissipation of eddy energy is not governed by one single mechanism, but instead by many different ones (Ferrari and Wunsch, 2009). Examples include, but are not limited to, eddy-wave interaction (Barkan et al., 2017), bottom drag (Huang

and Xu, 2018), and the western boundary graveyard effect (Zhai et al., 2010). This makes the task of finding a dissipation rate that encompasses all of these processes arduous, although an attempt has been made recently using ~~a numerical optimisation~~ an inverse method (Mak et al., 2022a). We believe tackling this problem from a theoretical stand point could be complimentary to the top-down approach employed by Mak et al. (2022a).

One important dissipation mechanism of eddy energy is relative wind stress, a process that can directly spin down mesoscale eddies by applying surface friction (Dewar and Flierl, 1987). Relative wind stress is described by

$$\boldsymbol{\tau}_{rel} = \rho_a C_d |\boldsymbol{u}_a - \boldsymbol{u}_0| (\boldsymbol{u}_a - \boldsymbol{u}_0) \,, \tag{2}$$

where ρ_a is air density, C_d is a drag coefficient that is a function of wind speed, $\boldsymbol{u}_a$ is the atmospheric wind 10 m above the ocean surface, and $\boldsymbol{u}_0$ are surface ocean velocities. Relative wind stress is termed so because it uses the relative motion between wind and ocean current velocities, $\boldsymbol{u}_a - \boldsymbol{u}_0$. In contrast, the absolute wind stress

$$\boldsymbol{\tau}_{rel} = \rho_a C_d |\boldsymbol{u}_a| \boldsymbol{u}_a \,, \tag{3}$$

neglects the ocean surface current, $\boldsymbol{u}_0$. The inclusion of the ocean surface current in (2) has led to improvements in estimating the wind power input into the large- and small- scale ocean circulation. For example, using relative wind stress has led to a 20-35% reduction in wind power input into the large-scale ocean circulation (Duhaut and Straub, 2006; Hughes and Wilson, 2008), a reduction in equatorial surface current speeds by 30% (Pacanowski, 1987), and damping of eddy kinetic energy by 10-30% (Zhai and Greatbatch, 2007; Munday and Zhai, 2015; Renault et al., 2016b). In a study by Rai et al. (2021), they examined eddy killing globally revealing relative wind stress to only damp length scales smaller than 260 km, whilst seasonal variations exhibited peaks in wintertime. Moreover, relative wind stress also influences the global climate system. Wu et al. (2017) looked at the decadal impact of relative wind stress in a global ocean model and found reductions in the ~~Atlantic Meridional Overturning Circulation~~ AMOC of around 13% as well as a 0.2 PW decrease in the maximum northward heat transport. Renault et al. (2016a) used a regional model to reveal relative wind stress ability in stabilising the Gulf Stream path, which was found later to be a result of reductions made to the forward and inverse cascade of energy (Renault et al., 2019). It is clear that relative wind stress does have a significant role in the global climate system and as such provides justification for ~~its use in this~~ the current work. A further justification comes from availability of ocean observations, meaning that we can utilise these data to infer a global map of the eddy energy dissipation rate.

In this paper we will derive a constrained eddy energy dissipation rate due to relative wind stress damping, validating this approach against a numerical model. In Sect. 2 we present theory used in this paper and also derive key analytical equations for the dissipation rate. Section 3 provides an overview of the experimental design. Section 4 looks at the evolution of total eddy energy in response to relative wind stress, comparing an analytical and numerical model. The dissipation rate is then presented in Sect. 5. Section 6 concludes the paper.

2 Theoretical framework

2.1 Deriving an expression for relative wind stress damping

The first objective of the theoretical framework is to derive an analytical expression that approximates the damping of eddy
energy due to relative wind stress. This can be done by making some assumptions on eddy shape and wind profile.

2.1.1 An idealised eddy

A comprehensive study by Chelton et al. (2011) revealed mesoscale eddies to have horizontal velocities that are in geostrophic
balance

$$\boldsymbol{u}_g = \frac{g}{f}\boldsymbol{k} \times \nabla_h \eta \, , \tag{4}$$

with a sea surface height field that is closely approximated by a Gaussian function

$$\eta(x,y) = Ae^{-(x^2+y^2)/R^2} \, . \tag{5}$$

In (4), $\boldsymbol{u}_g = (u_g, v_g)$ are horizontal geostrophic surface velocities in the zonal and meridional direction, respectively, g is the
gravitational acceleration constant, f is the Coriolis parameter, $\boldsymbol{k}$ is the vertical unit vector, ∇_h is the horizontal gradient
operator, and η is the sea surface height. In (5), A is the eddy amplitude, x and y are zonal and meridional coordinates, and
R is the eddy e-folding radius, which is the point of zero relative vorticity. The $\cdot_g$ in (4) implies geostrophic motion. Surface
velocities, $\boldsymbol{u}_g$, can then be found by putting (5) in (4), which give analytical velocities in the form

$$(u_g, v_g) = \Big(\frac{g}{f}\frac{2y}{R^2}, \underset{\sim}{-}\frac{g}{f}\frac{2x}{R^2} \Big)\eta \, . \tag{6}$$

The eddy described here exhibits a simple circular profile, as shown through sea surface height and relative vorticity in Fig.
1a,b.

2.1.2 Relative wind stress

Recall the bulk formula for relative wind stress in (2) given by

$$\boldsymbol{\tau}_{rel} = \rho_a C_d |\boldsymbol{u}_a - \boldsymbol{u}_g|(\boldsymbol{u}_a - \boldsymbol{u}_g) \, , \tag{7}$$

where only the geostrophic velocity component is employed to enable an analytical derivation. The drag coefficient C_d in Eq.
(7) is set as a constant value to keep the analytical theory simple. The relative wind stress formula in (7) can be simplified by
making use of the approximation due to Duhaut and Straub (2006) for the wind stress magnitude

$$|\boldsymbol{u}_a - \boldsymbol{u}_g| \approx |\boldsymbol{u}_a| - \boldsymbol{u}_g \cdot \boldsymbol{i} \, , \tag{8}$$

where $\boldsymbol{i}$ is a unit vector in the direction of the wind. This approximation is valid since we assume $|\boldsymbol{u}_a| \gg |\boldsymbol{u}_g|$. Equation (8) then
tells us that only the ocean current aligned with the wind contributes significantly to the wind stress magnitude. A wind profile
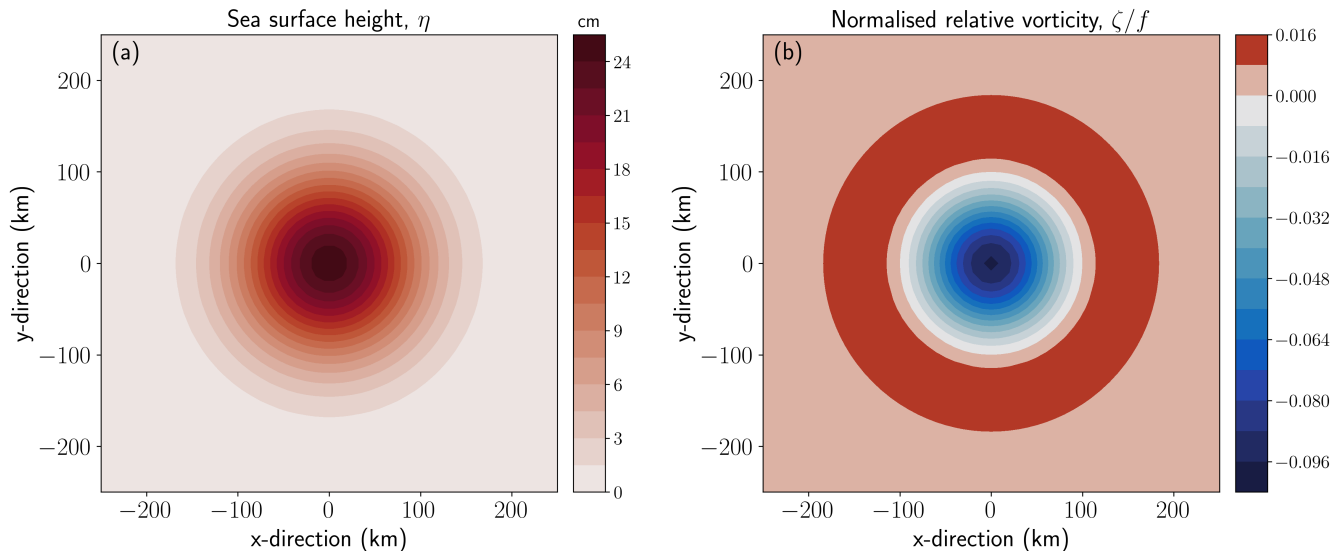
Figure 1. Idealised Gaussian eddy with anticyclonic rotation: a) sea surface height (in cm), and b) relative vorticity normalised by Coriolis parameter, f. Fields are calculated using parameters: $A = 25$ cm, $R = 100$ km, and $f = 10^{-4}$ s^{-1}.

for $\boldsymbol{u}_a$ is chosen to be uniform in space, blowing zonally west to east, with zero meridional component, i.e. $\boldsymbol{u}_a = (u_a, 0)$. This wind field represents a large-scale atmospheric wind with length scales larger than those of the mesoscale (Duhaut and Straub, 2006). The effect of the eddy current in relative wind stress is presented in Fig. 2a, which shows the difference in zonal wind stress, $\tau^x_{rel} - \tau^x_{abs}$. A dipole pattern of opposing values emerge at each meridional side of the eddy, where the largest values appear near to the eddy radius.

2.1.3 Wind power input

The next step in deriving the analytical expression for relative wind stress damping is to find the work done by winds on the surface geostrophic motion. This is done by taking the dot product of relative wind stress and surface geostrophic velocities, and making use of Eq. (8),

$$W_{rel} = \boldsymbol{\tau}_{rel} \cdot \boldsymbol{u}_g \,, \tag{9a}$$

$$= \rho_a C_d |\boldsymbol{u}_a - \boldsymbol{u}_g| (\boldsymbol{u}_a - \boldsymbol{u}_g) \cdot \boldsymbol{u}_g \,, \tag{9b}$$

$$= \rho_a C_d (|u_a| u_a u_g - |u_a| u_g^2 - u_a u_g^2 + u_g^3 - |u_a| v_g^2) \,. \tag{9c}$$

First, we can see the effect of relative wind stress on wind work in Fig. 2b by plotting the difference between relative and absolute wind work ($\boldsymbol{\tau}_{rel} \cdot \boldsymbol{u}_g - \boldsymbol{\tau}_{abs} \cdot \boldsymbol{u}_g$). Interpreting this wind work difference can be achieved by considering the values in Fig. 2a for an anticyclonic eddy (clockwise rotating). The negative wind stress difference in the north is multiplied by the positive anticyclonic eddy velocity, whilst the positive wind stress difference in the south is multiplied by the negative eddy

130 velocity, and thus the wind work difference is negative everywhere. This shows wind work by relative wind stress is a net sink for a uniform large-scale wind. So we expect an analytical expression for relative wind stress damping to be negative sign-definite. We recognise that other wind profiles could exist, though these have not been explored in this current work.

To find the analytical expression, we put analytical equations for geostrophic velocities (6) into Eq. (9c) and integrate over horizontal space in the limits of $x, y \rightarrow \pm\infty$

$$135 \quad P_{rel} = \int_{-\infty}^{\infty} \int_{-\infty}^{\infty} W_{rel}\, dx dy \,, \tag{10}$$

which gives

$$P_{rel} = -3\rho_a C_d |u_a| \frac{g^2 A^2 \pi}{2f^2} \,, \tag{11}$$

where P_{rel} has units kg m^2 s^{-3}. The analytical equation for relative wind stress damping found here in (11) is analogous to forms suggested by Gaube et al. (2015) and Jullien et al. (2020), although neither carried out a spatial integration. A
140 few things can be inferred from Eq. (11) on P_{rel}. First, P_{rel} depends on the magnitude of the wind velocity u_a, meaning that damping is independent of the wind direction. Second, P_{rel} is also independent of eddy polarity (sign of A) due to its quadratic dependence, implying that anticyclonic or cyclonic eddies will undergo equivalent damping when A is the same in absolute terms. We also see that P_{rel} does not depend on the eddy e-folding radius, R. This is because R cancels out in the integral limits of $\pm\infty$ for this circular eddy~~, whereby any gains in negative work due to R will be cancelled out by~~
145 ~~positive work~~. Finally, with all this in mind, P_{rel} is always negative, informing that relative wind stress will damp eddy energy. If wind power input were to be calculated using absolute wind stress in (3), its spatial integral would equal zero ($P_{abs} = 0$). Overall, this analytical finding is consistent with previous studies ~~(Xu et al., 2016; Renault et al., 2016b; Rai et al., 2021)~~ (Zhai and Greatbatch, 2007; Xu et al., 2016; Renault et al., 2016b; Rai et al., 2021) that find relative wind stress acts as a net sink of eddy energy.

2.2 Describing an analytical eddy

Mesoscale ocean eddies take on a complex vertical structure, making them hard to accurately model. However, studies such as the one by Wunsch (1997) allow us to make a reasonable choice in choosing a simple eddy model. An alternative choice could be made by using surface modes (de La Lama et al., 2016; LaCasce, 2017), though we discuss these in more detail in Sect. 6. Wunsch (1997) detailed the variability in eddy kinetic energy (EKE) in the vertical, and found EKE to exist primarily in the
155 barotropic and first baroclinic modes. These modes can be thought of in terms of their horizontal flow: the barotropic mode has flow that is completely depth-independent; and the first baroclinic mode has flow that is depth-dependent with a zero crossing at depth and zero net vertically-integrated flow. Over the global ocean, ~~Wunsch~~ Wunsch (1997) showed the first baroclinic mode contains the majority of EKE (60-70%), though in some regions, such as south of the Gulf Stream, strong barotropic mode signals were found. Nevertheless, links with the eddy sea surface height and their vertical structure have further been made. It
160 is now widely known that variations in eddy sea surface height reflect changes in the ocean's thermocline displacement, and
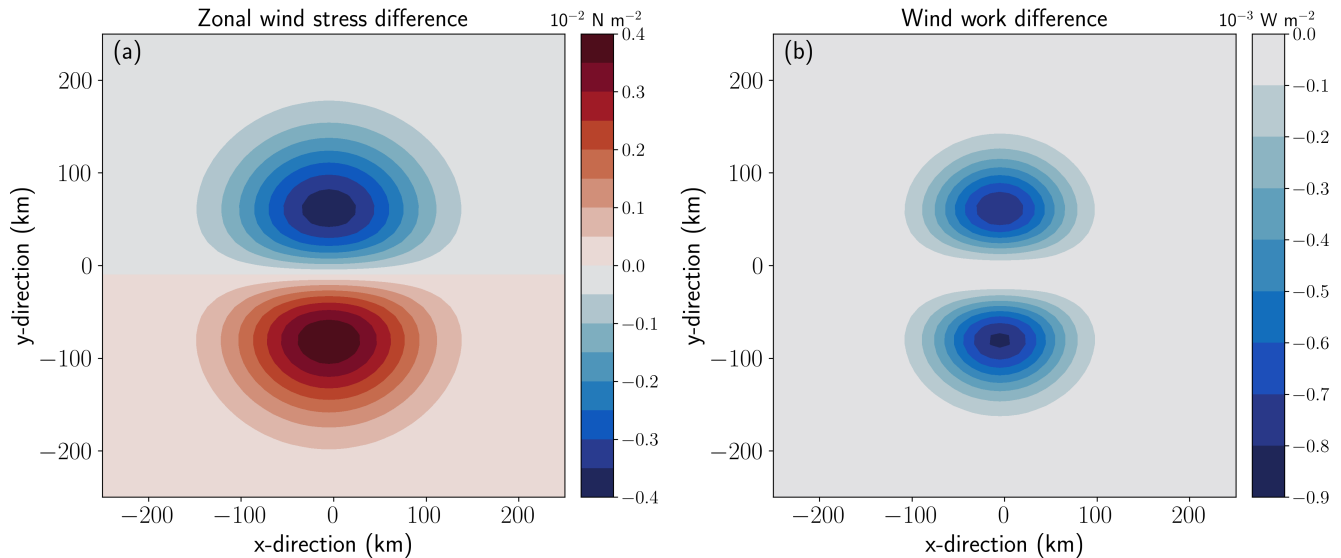
Figure 2. Horizontal plan views showing differences between relative and absolute wind stress calculated over an idealised Gaussian anticyclonic eddy: a) difference in zonal wind stress, $\tau_{rel}^x - \tau_{abs}^x$ (in units 10^{-2} N m^{-2}), and b) difference in wind work, $W_{rel} - W_{abs}$ (in units 10^{-3} W m^{-2}). Fields are calculated using parameters: $A = 25$ cm, $R = 100$ km, $f = 10^{-4}$ s^{-1}, $u_a = 7$ m s^{-1}, $C_d = 1.1 \times 10^{-3}$, and $\rho_a = 1.2$ kg m^{-3}. ~~Relative wind stress is computed using the full expression in Eq.~~ (7).

thus changes in first baroclinic mode eddy energy (Smith and Vallis, 2001). In this work~~we proceed with the representation of a singular~~, we proceed, for simplicity, by representing an eddy using only the first baroclinic mode~~eddy for simplicity~~.

2.2.1 Baroclinic eddy

Two-layer shallow water equations are used to describe the baroclinic eddy

165

$$\frac{D\boldsymbol{u}_{g1}}{Dt} + f\boldsymbol{k} \times \boldsymbol{u}_{g1} = -g\nabla_h(\eta_1) + \frac{\boldsymbol{\tau}}{\rho_0 h_1} \,, \tag{12a}$$

$$\frac{D\boldsymbol{u}_{g2}}{Dt} + f\boldsymbol{k} \times \boldsymbol{u}_{g2} = -g\nabla_h(\eta_1) - g'\nabla_h(\eta_2) \,, \tag{12b}$$

$$\frac{\partial h_1}{\partial t} + \nabla_h \cdot (h_1 \boldsymbol{u}_{g1}) = 0 \,, \tag{12c}$$

$$\frac{\partial h_2}{\partial t} + \nabla_h \cdot (h_2 \boldsymbol{u}_{g2}) = 0 \,, \tag{12d}$$

where $\cdot_{1,2}$ denotes the upper and lower layer variables, η_2 is the interface displacement between the two layers, which is measured positive upwards, $g' = g(\rho_2 - \rho_1)/\rho_2$ is the reduced gravity - change in acceleration of gravity due to buoyant forces - found using upper and lower layer density, and $h_1 = H_1 + \eta_1 - \eta_2$ and $h_2 = H_2 + \eta_2$ are the respective layer depths of which $H_{1,2}$ is the reference layer depth. This two-layer model includes the effects of stratification through g', which accounts for the

170

adjustment between the two layers due to the change in density. Equations (12a) and (12b) are momentum equations and Eqs. (12c) and (12d) are continuity equations. The second term on the right hand side of Eq. (12a) is the wind forcing.

175   Before progressing with the derivation of the baroclinic eddy energy equation, some points are discussed first. The two-layer shallow water equations in the form shown in (12) do not immediately describe the baroclinic eddy, rather an ocean with two layers of differing density. It is known that the sea surface height typically reflects the displacement of the main thermocline (Wunsch, 1997). In this case, there exists proportionality between the upper and lower layers in the two-layer analytical model, and as such the vertical structure of the baroclinic eddy can be described. Following Cushman-Roisin and Beckers (2006), $\eta_1 =$

180    $\mu\eta_2$ and $\boldsymbol{u}_2 = \lambda\boldsymbol{u}_1$, where μ and λ are proportionality coefficients to be defined, which both provide the dynamical structure of the eddy through normal modes. Normal modes exhibit wave patterns that depend on these proportionality coefficients, and these are found as follows. Equating together the momentum equations (12b) with (12a) and neglecting wind stress gives

$$\lambda = \frac{g\mu + g'}{g\mu} \,, \tag{13}$$

then equating the continuity equations (12d) with (12c) gives

185    $$\frac{1}{\mu - 1} = \frac{H_2\lambda}{H_1} \,. \tag{14}$$

A quadratic equation for λ can be found from (13) and (14)

$$H_2\lambda^2 + (H_1 - H_2)\lambda - H_1 = 0 \,, \tag{15}$$

~~where solutions are only valid for $g'/g \to 0$.~~ In (15), there are two solutions for λ that relate to the barotropic (BT) and first baroclinic mode (BC1). ~~The~~ In the limit $g'/g \to 0$, the BT is described by $\lambda = 1$ and $\mu = H/H_2$, and BC1 is given by

190    $\lambda = -H_1/H_2$ and $\mu = -g'H_2/gH$. A baroclinic eddy is therefore represented by the two-layer model through the use of BC1's λ and μ. Whilst H_1 is the depth of the upper layer, in BC1 this can also be defined as the first baroclinic mode zero crossing. An example of this mode can be seen in Fig. 1 of Wunsch (1997).

2.2.2 Eddy energy equation

The derivation of the two-layer energy equation is done as follows. Equation (12a) is multiplied by $h_1\boldsymbol{u}_{g1}$, (12b) by $h_2\boldsymbol{u}_{g2}$,

195   (12c) by $g\eta_1$, and (12d) by $g'\eta_2$, giving the upper and lower layer kinetic and potential energy equations, respectively. The resulting equations are added together to give the total eddy energy equation for an analytical baroclinic eddy

$$
\begin{aligned}
\frac{\partial}{\partial t}\Big(\rho_0\big(h_1\frac{1}{2}\boldsymbol{u}_{g1}\cdot\boldsymbol{u}_{g1} + h_2\frac{1}{2}\boldsymbol{u}_{g2}\cdot\boldsymbol{u}_{g2} + \frac{1}{2}g\eta_1^2 + \frac{1}{2}g'\eta_2^2\big)\Big) + \\
\nabla_h\cdot\Big(\rho_0(\frac{1}{2}\boldsymbol{u}_{g1}\cdot\boldsymbol{u}_{g1} + g\eta_1)h_1\boldsymbol{u}_{g1} + \rho_0(\frac{1}{2}\boldsymbol{u}_{g2}\cdot\boldsymbol{u}_{g2} + g\eta_1 + g'\eta_2)h_2\boldsymbol{u}_{g2}\Big) \\
= \boldsymbol{\tau}\cdot\boldsymbol{u}_{g1} \,.
\end{aligned}
\tag{16}
$$

In Eq. (16), terms in the top row in order of left to right are: upper layer kinetic energy, lower layer kinetic energy, upper layer potential energy, and lower layer potential energy. Terms in the middle represent the divergence of kinetic and potential energy, as well as divergence of pressure work. In the bottom row: work done by winds on the surface geostrophic motion.

We now want to acquire an analytical equation for (16) that we can use to approximate the damping of eddy energy by relative wind stress. To achieve this, Eq. (16) is integrated over space using analytical terms for $\eta_{1,2}$ and $\boldsymbol{u}_{g1,2}$, where the upper layer terms are given in (5) and (6), and the lower layer terms are found using the proportionality coefficients μ and λ. First, the combined kinetic and potential energy term from the top row of (16) leads to the following analytical form

205

$$(KE + PE)_{bc} \equiv E = \rho_0 \pi \left(\left((H_1 - \lambda^2 H_1 + \lambda^2 H) \frac{g^2}{2f^2} + R^2 \frac{g}{4} + R^2 \frac{g\prime}{4\mu^2} \right) A^2 + \left((1 - \frac{1}{\mu} + \frac{\lambda^2}{\mu}) \frac{2g^2}{9f^2} \right) A^3 \right) , \tag{17}$$

which is measured in units of $\mathrm{kg\ m^2\ s^{-2}}$. Of the two terms that contain R, the second one makes up the available potential energy from the lower layer. Since the terms in the middle row of (16) represent the divergence of energy flux in the domain, under no normal flow boundary conditions the integral of this term is zero. Next, the integral of the first term in the bottom row of (16) is the wind power input, previously derived in Sect. 2.1.

210   After integrating Eq. (16) we arrive at an equation in the form

$$\frac{\partial}{\partial t}(KE + PE)_{bc} = P , \tag{18}$$

where $(KE + PE)_{bc}$ is combined baroclinic kinetic and potential energy per unit volume, and P is wind power input. Equation (18) now depends on a few key eddy parameters, in particular eddy amplitude, A. For a geostrophic eddy, this means we can take its amplitude and infer the evolution of total eddy energy in response to relative wind stress damping. To do this, the energy

215   equation (18) is integrated forward in time using a fourth-order Runge-Kutta scheme for the first two time steps ($n = 2, 3$), followed by a third-order Adams-Bashforth scheme for time steps $n = 4, \cdots$. The Adams-Bashforth scheme is employed to match that used in the MITgcm. Once total eddy energy is found at the next time step $n + 1$, eddy amplitude A is recovered from eddy energy E in (17) through a Newton-Raphson root finder method. The time evolution of analytical eddy energy is then compared with a numerical model in Sect. 4.

3 Experimental design

3.1 Numerical configuration

The numerical experiments were performed using the hydrostatic MIT general circulation model (Marshall et al., 1997a, b). Employing this numerical model is done so we can verify whether the analytical wind power input derived in Sect. 2.1 can sufficiently predict the decay of baroclinic eddy energy due to relative wind stress. The numerical setup was described in detail

225   in Wilder et al. (2022), though we describe some pertinent details along with our attempt to design a continuously stratified model that displays similar characteristics to the analytical two-layer model.

The numerical model is set up on an f-plane in a box-like domain spanning $2000\ \mathrm{km}$ in each x and y direction with equal grid spacing of $10\ \mathrm{km}$. The ocean is $4000\ \mathrm{m}$ deep and the vertical grid has 91 z-levels with spacing of $5\ \mathrm{m}$ at the surface and 100 m at depth. The ocean bottom is flat and a free-slip boundary condition is used, along with no bottom drag. Neglecting bottom

230   drag may have repercussions for the cascade of eddy energy (Scott and Arbic, 2007), however, its neglect means damping by

relative wind stress can be isolated in our model. A grid-scale biharmonic viscosity is used for numerical stability purposes as well as to parameterise the dissipation of energy at the smallest of scales.

The baroclinic eddy is initialised using analytical equations. The stratification is given by a 3D temperature field of the form

235
$$T(x,y,z) = T' e^{-(x^2+y^2)/R^2} e^{-\gamma(z/H_1)} + T_{ref}(z)\,, \tag{19}$$

where T' is the temperature anomaly, γ ~~governs~~ influences the stratification of the water column, z are vertical grid levels measured positive downward, and H_1 is the ~~point of zero crossing for horizontal velocities~~thermocline depth. The background temperature T_{ref} is derived using the linear equation of state from a reference background density given by

$$\rho_{ref}(z) = \rho_0(1 - N_0^2(z/g)) + 0.5\Delta\rho(1 - \tanh(B(z+H_1)/H))\,, \tag{20}$$

240 where ρ_0 is a reference density, N_0 is a reference buoyancy frequency, $\Delta\rho$ is the difference in density between the surface and bottom, B is the gradient of the density profile, and H is the depth of the ocean. Horizontal velocities are in thermal wind balance

$$\boldsymbol{u}_g(x,y,z) = \frac{g}{f}\boldsymbol{k} \times \left(\nabla\eta + \alpha \int\limits_z^0 \nabla T\, dz \right)\,, \tag{21}$$

where $\boldsymbol{u}_g = (u_g, v_g)$ are zonal and meridional geostrophic velocity components, and α is the thermal expansion coefficient. In
245 (21), the first term in the brackets is surface velocity derived from sea surface height, and the second term is vertical velocity shear derived from thermal wind balance.

So that an adequate comparison of the two-layer baroclinic eddy in Sect. 2.2.1 can be made with the stratified model described here, a few parameters in (19) and (20) need to be tuned appropriately. In the two-layer model, the first baroclinic mode has zero net vertically-integrated flow in the horizontal, ~~that is~~ where H_1 is the point where horizontal velocities are zero.
250 This means that flow in the upper layer is countered by an opposing lower layer flow, ~~meaning~~ defined by

$$\int\limits_{-H}^0 \boldsymbol{u}_g\, dz = 0\,. \tag{22}$$

We minimise net flow in the stratified model by tuning parameters A, T', γ, and B. The aim is to achieve a minimal net flow and also have similar eddy properties between each setup, e.g. layer depths and sea surface height. We find the horizontal net flow in the MITgcm is close to ~~, but not~~ zero. This implies the presence of a barotropic mode component in this setup, which is
255 not too dissimilar to the real ocean (Wunsch, 1997; Arbic and Flierl, 2004). Some key model parameters are shown in Table 1.

The wind field used in this setup is uniform in one direction and is designed to represent a large-scale background wind~~.~~ ~~See~~; see Wilder et al. (2022) for further details on the wind setup. The drag coefficient in the wind stress formula is a function of the magnitude of the wind speed (Large and Pond, 1981), which is different to the analytical model where C_d is constant. However, the differences in drag coefficient are not expected to cause large differences between the total wind damping in the
260 numerical and analytical models (Wilder, 2022).

When the model is first initialised it is allowed to run for 10 days with zero wind forcing. This allows any inertial waves to die down, and also let the equations of motion form a balance that could be slightly different to geostrophy. After this adjustment phase, the wind forcing is turned on and the model is run for 400 days.

Table 1. Key experimental parameters

Symbol	Value	Description
H	4000 m	Ocean depth
$\Delta x, y$	10 km	Horizontal grid resolution
f	$9.3461 \times 10^{-5} \text{ s}^{-1}$	Coriolis frequency
A	25 cm	Eddy amplitude
R	100 km	Eddy e-folding radius
$\boldsymbol{u}_a$	7 m s^{-1}	Wind speed
C_d	1.1×10^{-3}	Drag coefficient
ρ_a	1.2 kg m^{-3}	Air density
ρ_0	1026 kg m^{-3}	Reference ocean density
T'	2.5 °C	Temperature anomaly
γ, B	1, 3	Stratification parameters
$\Delta \rho$	3 kg m^{-3}	Density difference
N_0	10^{-5} s^{-1}	Reference buoyancy frequency
H_1	800 m	Upper layer/BC1 zero crossing depth
ρ_2	1026.9 kg m^{-3}	Analytical lower layer density

3.2 Diagnosing model energetics

To validate the evolution of baroclinic eddy energy in the analytical model (Sec. 2.2.1), time-mean quantities of kinetic and potential energy, and wind damping for the continuously stratified MITgcm model need to be defined. The following are mean potential energy, mean kinetic energy, and wind power input

$$PE = -\int_V \frac{g}{2n_0(z)} \overline{\rho^*(x,y,z,t)}^2 \, dV \,, \quad \text{and} \tag{23}$$

$$KE = \int_V \frac{\rho_0}{2} \left(\overline{u}_g^2 + \overline{v}_g^2 \right) dV \,, \tag{24}$$

$$P = \int_S \overline{\boldsymbol{\tau}} \cdot \overline{\boldsymbol{u}}_g \, dS \,, \tag{25}$$

where $\bar{\cdot}$ represents a 16 day time-mean, $\rho^*(x,y,z,t) = \rho(x,y,z,t) - \rho_{ref}(z)$ is a density anomaly relative to a constant-in-time reference background density state, $n_0(z)$ is the vertical gradient of $\rho_{ref}(z)$, u_g and v_g are geostrophic velocity components in the zonal and meridional direction, and $\int_V$ is a volume integral. The density field $\rho(x,y,z,t)$ is computed from the MITgcm

temperature field, and $\rho_{ref}(z)$ is given in Eq. (20). The use of potential energy anomaly informs how much potential energy can be converted into kinetic energy, as opposed to how much potential energy exists within the stratification. Choosing the potential energy definition in (23) implies a quasi-geostrophic framework and has been used in past studies (von Storch et al., 2012; Chen et al., 2014; Youngs et al., 2017).

3.3 Setting up the analytical model

The time evolution of analytical eddy energy is achieved by time-stepping Eq. (18) forward in time. To begin the time-stepping of the analytical model, initial eddy energy and dissipation is found by using data from the MITgcm model run, such as eddy amplitude. Equivalent eddy energy is desired to visualise the rate of decay imposed by relative wind stress. Because the MITgcm setup has been chosen to display similar characteristics to the analytical model, the energetics are thus fixed. To make eddy energy in the analytical model match the MITgcm setup, we modify the analytical lower layer density until potential energy matches (see Table 1). Kinetic energy is only a small fraction of total eddy energy, so there is less importance in matching this quantity between the analytical and numerical setups. Overall, these details allow us to make a consistent comparison between both setups, and examine more clearly the rate of eddy energy decay by relative wind stress.

4 Verifying the analytical model

In this section we present our first set of results, comparing the time evolution of the analytical and numerical eddy energy budgets. Figure 3 shows a time-series of domain integrated eddy energy ($KE + PE$) for an anticyclonic (ACE) and cyclonic (CE) eddy. The first thing that can be seen is the initial offset in total eddy energy between the analytical model (Pred) and the numerical model (MIT) in ACE and CE. Here, potential energy is being matched between the analytical and numerical model, and therefore the discrepancy implies that the kinetic energy contribution is not equivalent between Pred and MIT. This kinetic energy mismatch is expected since the two-layer analytical eddy cannot realistically represent the continuously stratified MITgcm eddy.

~~Now, focusing~~ We first focus on the first 150 days of the ACE (Fig. 3a). In the absolute wind stress case (AW), AW MIT is damped by 0.1 PJ up to day 150, while AW Pred sees zero energy loss due to absolute wind stress not damping the eddy. In the relative wind stress case (RW), the negative wind power input (Fig. 5a) is able to remove eddy energy from RW Pred and RW MIT. Up to day 150, RW Pred loses 0.38 PJ whilst RW MIT loses around 0.4 PJ, relative to day 31 in RW time-series. This damping by relative wind stress is similar because the wind power input in Pred and MIT is around -3×10^7 W.

Beyond day 150, Pred and MIT time-series begin to diverge, with MIT undergoing a sudden reduction in total energy of around 10% over 30 days, whilst Pred continues with a smooth decay. This divergence indicates that MIT is no longer evolving as it initially did, suggesting the eddy is undergoing an instability process and departing from its initial state. In RW, this sudden reduction in total energy also takes place at an earlier timescale. These possible instabilities may also impact the relative wind power input, since P_{rel} displays a sharp increase in negative wind power input (Fig. 5). An in depth examination of the anticyclonic eddy response can be found in Wilder et al. (2022), and so the finer details are omitted from this discussion.
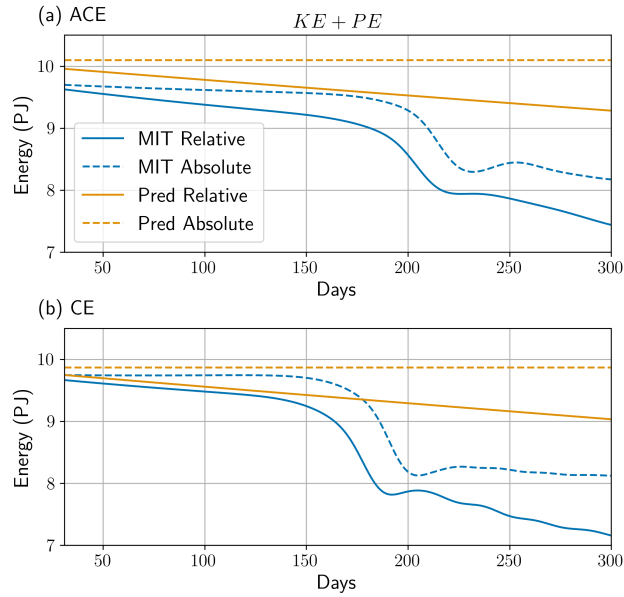
Figure 3. Time-series of total eddy energy, E for: a) anticyclone, and b) cyclone. In figure legend, MITgcm given by either MIT Relative / Absolute and analytical model given by either Pred Relative / Absolute. Units of energy in PJ. MITgcm values are 16 day time-means.

From day 250, the rate of decay in MIT slows for each wind stress and is much more closely aligned with the decay rate in Pred. Inspecting the ACE eddy surface relative vorticity in Fig. 4 illustrates the regime change of the eddy, consistent with the changes seen in the time-series (Fig. 3). The ACE under AW and RW is initially coherent at day 125 (Fig. 4a,d), then develops two outer lobes of stronger cyclonic vorticity by day 200 (Fig. 4b,e), before eventually splitting into two separate anticyclonic eddies by day 275 (Fig. 4c,f). This process of eddy splitting in baroclinic eddies has been well documented in previous studies (Ikeda, 1981; Dewar et al., 1999), where time-scales vary with parameter values chosen (Mahdinia et al., 2017).

Similar results are also observed for the CE (Fig. 3b). The decay rate in total energy follows roughly the same trajectory as the ACE up to 150 days, with more damping taking place in RW Pred and RW MIT due to negative wind power input (Fig. 5b). As discussed earlier, wind power input due to relative wind stress is independent of eddy polarity, so no bias in damping rate should exist. Up to day 130 of the time-series, RW Pred is damped by 0.37 PJ, and RW MIT is damped by 0.26 PJ. The disparity in damping is not a result of unequal dissipation rates by P_{rel} (Fig. 5b), but is a result of energy production in MIT via vertical diffusive processes. Indeed, running a simulation with no eddy, no wind, but with vertical diffusion did result in potential energy production (not shown). However, why this is more prominent in the cyclonic eddy than anticyclonic has not been investigated further. After day 150, MIT exhibits a sudden reduction in total energy with each wind stress, which happens earlier in RW. Moreover, in contrast to the ACE, the timescale for this sudden reduction to take place in the CE is around 15-20% shorter. This points to an anticyclone-cyclone asymmetry, which has been recognised in past studies (Chelton et al., 2011; Mkhinini et al., 2014; Mahdinia et al., 2017).
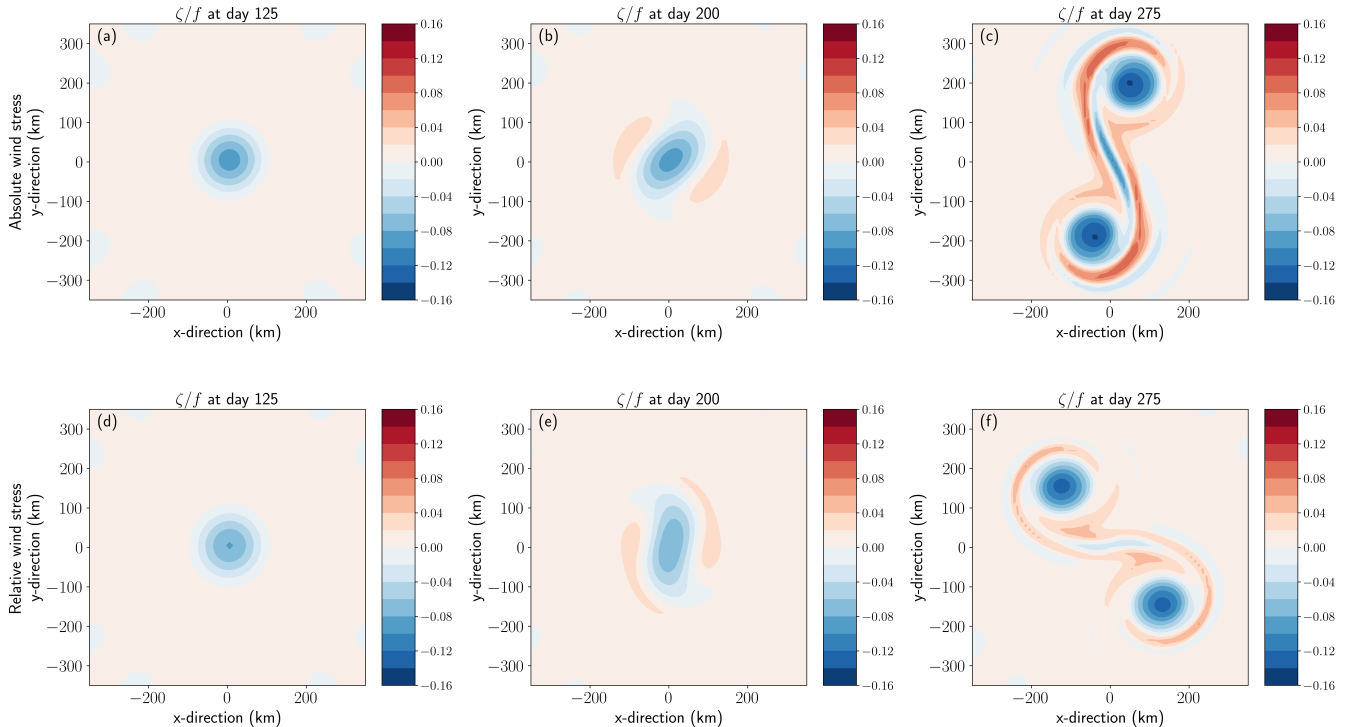
Figure 4. Horizontal plan views of MITgcm surface geostrophic relative vorticity normalised by Coriolis frequency in an anticyclonic eddy for absolute (top) and relative (bottom) wind stress at days: a,d) 125, b,e) 200, and c,f) 275. Fields are calculated using daily mean SSH output from MITgcm simulations.

In this section we have compared the evolution of total eddy energy between an analytical and numerical model. The results tell us that a two-layer analytical model can reasonably explain the evolution of total eddy energy in the MIT simulation. However, the agreement between both models diminishes due to an instability process in the MIT simulation. Nevertheless, we find the time-scale of around ~ 150 days for eddy energy agreement to be acceptable, and as such feel confident to propose a constrained eddy energy dissipation rate in Sect. 5.

5 A constrained dissipation rate

An eddy energy dissipation rate due to relative wind stress takes the form

$$\Lambda_{rel} = |P_{rel}|/E, \tag{26}$$

and can be found by putting the analytical equations for P_{rel} from (11) and E from (17) into the above for a constrained Λ_{rel}. Since the analytical eddy energy E is made up of several terms, we will simplify E by finding its dominant term. A simple scaling of Eq. (17) shows potential energy within the thermocline to be the dominant term. For this we choose typical parameter
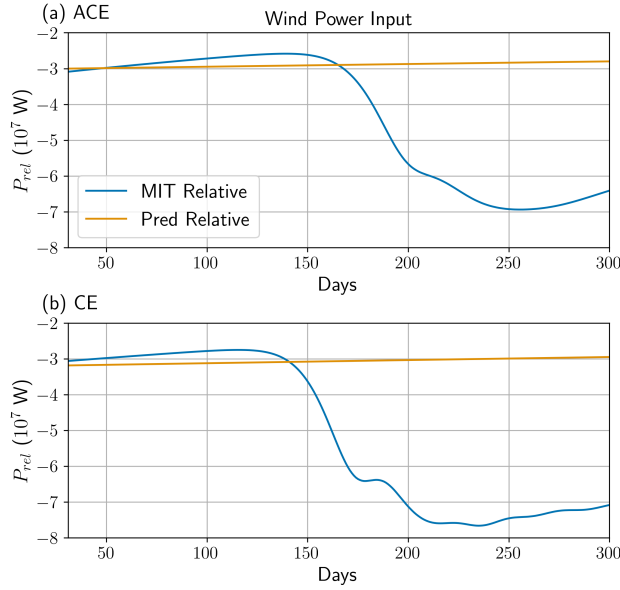
Figure 5. Time-series of total wind power input in relative wind stress simulation, P_{rel} for: a) anticyclone and b) cyclone. In figure legend, MITgcm given by MIT Relative and analytical model given by Pred Relative. Units of power in W. MITgcm values are 16 day time-means.

values: $H = 4000$ m, $H_1 = 800$ m, $\rho_1 = 1026$ kg m^{-3}, $\rho_2 = 1029$ kg m^{-3}, $R = 100$ km, and $f = 10^{-4}$ s^{-1}. Putting these values into Eq. (17) gives an approximation to eddy energy as

$$E \approx \rho_0 \pi \frac{R^2 g\prime A^2}{4\mu^2} \,. \tag{27}$$

Moreover, it is also well known that potential energy is greater than kinetic energy when the scale of motions exceed the first baroclinic radius of deformation (Gill et al., 1974). As such, mesoscale eddies will have potential energy much greater than kinetic energy. Furthermore, for this dissipation rate to be formed of potential energy, we are also arguing that relative wind stress has an immediate effect on the dissipation of potential energy, and there are no delays in the timescale of this communication. While relative wind stress directly damps eddy surface motions, Wilder et al. (2022) show that relative wind stress simultaneously releases potential energy via wind-induced baroclinic conversion. Therefore, the dissipation rate of eddy energy (27) due to relative wind stress (11) can take the form

$$\Lambda_{rel} \approx \frac{6\rho_a C_d |u_a| g^2 \mu^2}{\rho_0 R^2 g\prime f^2} \,. \tag{28}$$

The dissipation rate Λ_{rel} is independent of eddy amplitude due to P_{rel} and E being functions of A^2. We see instead that Λ_{rel} depends on a few terms that can vary in space, such as the magnitude of wind velocity $|u_a|$, proportionality coefficient μ, eddy length scale R, and reduced gravity $g\prime$. ~~In~~ It is worth pointing out that in the limit of $H_1/H_2 \to 0$ and $\mu \to g\prime/g$, such as in the 1.5-layer model (Vallis, 2017), (28) further simplifies to

$$\Lambda_{rel} \approx \frac{6\rho_a C_d |u_a| g\prime}{\rho_0 R^2 f^2} \,, \tag{29}$$

350 which clearly shows the importance of g' for determining the dissipation rate. We proceed with Eq. (28) throughout Sec. 5. In addition, we now consider *eddies* to be deviations from the time-mean, rather than just being a singular coherent eddy. The interpretation of the dissipation rate can also be thought of as one for these eddy time-mean deviations.

5.1 Calculating the dissipation rate

We approach the computation of the dissipation rate Λ_{rel} in Eq. (28) by acquiring datasets for $|\boldsymbol{u}_a|$, μ, R, and g'. Wind data
355 is now assumed to be the wind speed $|\boldsymbol{u}_a|$, rather than just the zonal wind velocity component $|u_a|$, because wind patterns vary in latitude and longitude over the global ocean. Wind speed is taken from the NCEP-NCAR Reanalysis 1 data (Kalnay et al., 1996) and is on a 2 degree horizontal grid. The wind speed data is then interpolated onto a 1 degree horizontal grid. The remaining terms require temperature and salinity datasets, and these are taken from World Ocean Atlas (Locarnini et al., 2019; Zweng et al., 2019) on a 1 degree horizontal grid. Each dataset is made up of long term monthly means over the period 1981 to
360 2010, which are averaged into seasons June-July-August (JJA) and December-January-February (DJF). The terms μ and g' are found by solving a Sturm-Liouville eigenvalue problem for the first baroclinic mode using the temperature and salinity fields (see Sect. 5.1.1). Arriving at an approximation for the eddy length scale R comes with some uncertainty, and for this reason we establish two forms for R. As a result, we will also form two choices for the dissipation rate that will indicate where we might expect the value to fall between. From the eigenvalue problem (Sect. 5.1.1), the first baroclinic Rossby radius of deformation,
365 R_d can be found, which we take as one choice for R. Another choice for R is found by scaling our computed R_d with data from Chelton et al. (2011), Fig. 12, where an e-folding radius L_e, and Rossby radius $\hat{R}_d$, are presented over latitude as zonal averages. That is, our values of R are given as either R_d or $(L_e/\hat{R}_d)R_d$.

5.1.1 The eigenvalue problem

Following Xu et al. (2011), the eigenvalue problem takes the form

370
$$\frac{d}{dz}\left(\frac{f^2}{N^2}\frac{d\phi_n(z)}{dz}\right) + \lambda_n\phi_n(z) = 0, \tag{30}$$

with boundary conditions

$$\left(\frac{1}{N^2}\right)\frac{d\phi}{dz} = 0 \quad \text{at } z = 0, -H, \tag{31}$$

where $\phi_n(z)$ is the eigenmode, λ_n is the eigenvalue, $N(z) = -(g/\rho_0)\partial\rho'(x,y,z)/\partial z$ is the buoyancy frequency, $\rho'(x,y,z)$ is a density anomaly with respect to a reference ocean density, ρ_0. Here, λ_n is not the same as λ defined in Sect. 2.2.1, and H is
375 the depth of the ocean taken from the World Ocean Atlas datasets, not the value given in Table 1, and so varies in space. The subscript $\cdot_n$ is the nth mode. The Gibbs SeaWater Oceanographic Toolbox (McDougall and Barker, 2011) is used to calculate ρ. The eigenvalue problem (30) is solved using the MATLAB function *dynmodes.m* (Klinck, 2009), and ocean depths locations where the ocean depth is shallower than 300 m are neglected not considered. From Flierl (1978), the first baroclinic Rossby radius of deformation is related to the eigenvalue like by, $R_d = 1/\sqrt{\lambda_1}$. We subsequently use R_d as one of our choices for the

length scale of mesoscale eddies. We take the depth of zero crossing of the first baroclinic mode to be H_1. The eigenmode is normalised using

$$\int_{-H}^{0} \phi_i \phi_j \, dz = H \delta_{ij} \, . \tag{32}$$

Reduced gravity is defined from Xu et al. (2011) as $g' = f^2 (1 + \phi_1^2(0))/\lambda_1 H_2$. The coefficient μ is defined as previously in Sect. 2.2.1 and is quantified by using the calculated terms g' and H_1.

5.1.2 The contributing terms

Figure 6 displays the terms $|\boldsymbol{u}_a|$, μ, and g' over the global ocean. Figure 6a,b illustrate the wide variability in space and time for the wind speed. There is a clear increase in $|\boldsymbol{u}_a|$ at higher latitudes during each hemispheric winter, while there is a slow down in winds during their summer. The largest wind speeds occur around 90°E in the Southern Ocean, whilst the western boundaries see values a few m s^{-1} ~~slower~~ lower. In the μ term, there is a slight variation between seasons, with the largest absolute values over the equatorial regions (Fig. 6c,d). The spatial pattern between g' (Fig. 6e,f) and μ is similar due to μ depending on g'. Across each season, g' remains fairly consistent over the equatorial bands. At higher latitudes, g' varies due to changes in seasonal stratification.

Figure 7 displays the Rossby radius of deformation (R_d) and e-folding scale ($(L_e/\hat{R}_d)R_d$) used to define the eddy length scale, R. Figure 7a,b shows R_d, similar to Fig. 6 in Chelton et al. (1998), whereby it decreases in length scale with increasing latitude (~ 200 km to ~ 10 km). The e-folding length scale L_e is shown in Fig. 7c,d and similarly varies in latitude, with the largest (smallest) length scales at low (high) latitudes. Comparing R_d and $(L_e/\hat{R}_d)R_d$, we see that the latter is around 3-4 times bigger than R_d across much of the ocean. Nevertheless, both length scales are within the eddy killing scale of 260 km found by Rai et al. (2021). Over JJA and DJF periods, there is very little seasonal variability. The region ~~over~~ between 5°S ~~to~~ and 5°N has been masked due to the Coriolis parameter tending to zero at the equator.

5.2 A global dissipation rate

A global dissipation rate is now presented, culminating from the variable climatology data calculated in Sect. 5.1, along with values from Table 1. Figure 8 shows $\log_{10}(\Lambda_{rel}/10^{-7} \text{ s}^{-1})$ over the global ocean, making it clear where Λ_{rel} could be important for eddy energy dissipation. We compare Λ_{rel} with a constant value of 10^{-7} s^{-1} because the latter has been used in several past studies (Mak et al., 2017, 2018). Each dissipation rate is shown using R_d or $(L_e/\hat{R}_d)R_d$ for eddy length scale, R.

Beginning with the Rossby radius of deformation R_d, we find $\log_{10}(\Lambda_{rel}/10^{-7} \text{ s}^{-1})$ is largely positive across the global ocean in each season (Fig. 8a,b). In the Southern Ocean we find large values throughout, with Λ_{rel} being up to 4 times that of 10^{-7} s^{-1}. This region is known to exhibit important bathymetric features, which impose a control on the Southern Ocean flow (Graham et al., 2012; Munday et al., 2015). For example, the transition from small to large values at 60°W could be in part due to the bathymetry of Drake Passage. We can also see that R_d becomes smaller moving from 120°W to 0° (Fig. 7a,b), contributing to the increase in dissipation rate owing to smaller levels of available potential energy. In the Northwest
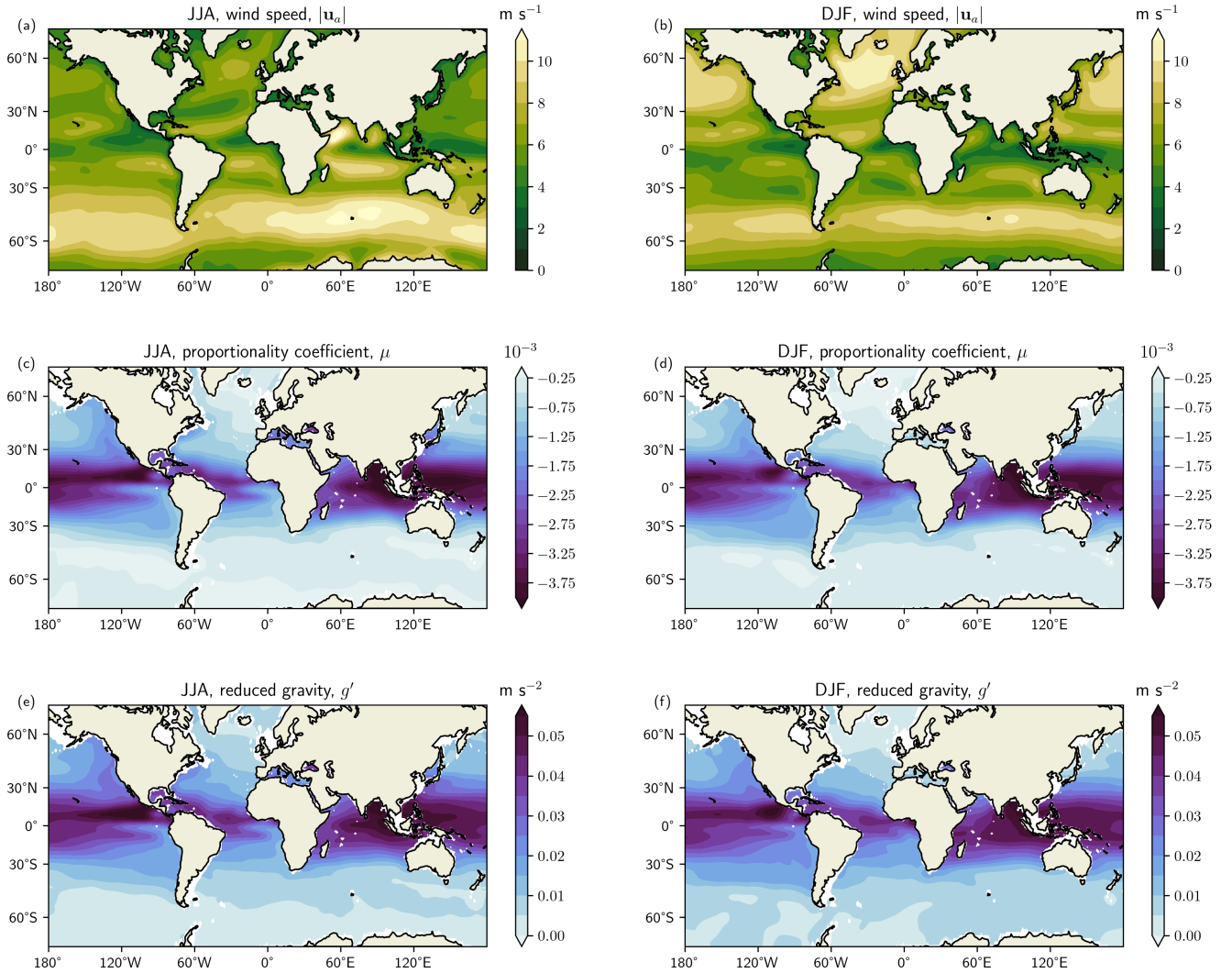
Figure 6. Global maps between the latitudes of 70°S and 70°N displaying contributions to the dissipation rate, Λ_{rel} for: left) JJA; and right) DJF. In a,b), wind speed, $|\boldsymbol{u}_a|$ (in units $\mathrm{m\,s}^{-1}$), c,d) proportionality coefficient, μ, and e,f) reduced gravity, g' (in units $\mathrm{m\,s}^{-2}$). The data is calculated from World Ocean Atlas and NOAA datasets over 1981-2010 period.

Atlantic, we see that the zero contour of $\log_{10}(\Lambda_{rel}/10^{-7}\,\mathrm{s}^{-1})$ roughly follows the jets separation past Cape Hatteras. Here, the dissipation rate by relative wind stress is similar to the value posed in Mak et al. (2018). From the coast to the basin interior we see that Λ_{rel} reduces in size, most likely due to ~~reductions~~ an increase in R_d and reduction in $|\boldsymbol{u}_a|$, while changes in g' and μ contribute less to this change due to their smaller changes (Figs. 7a,b and 6). It was shown in Mak et al. (2022a, b) through their global simulations that the western boundary currents display ~~weaker eddy energy . This is suggested to be because~~ too weak eddy energy when employing their dissipation rate of $10^{-7}\,\mathrm{s}^{-1}$ ~~is too high, and as such the~~ . This dissipation rate is
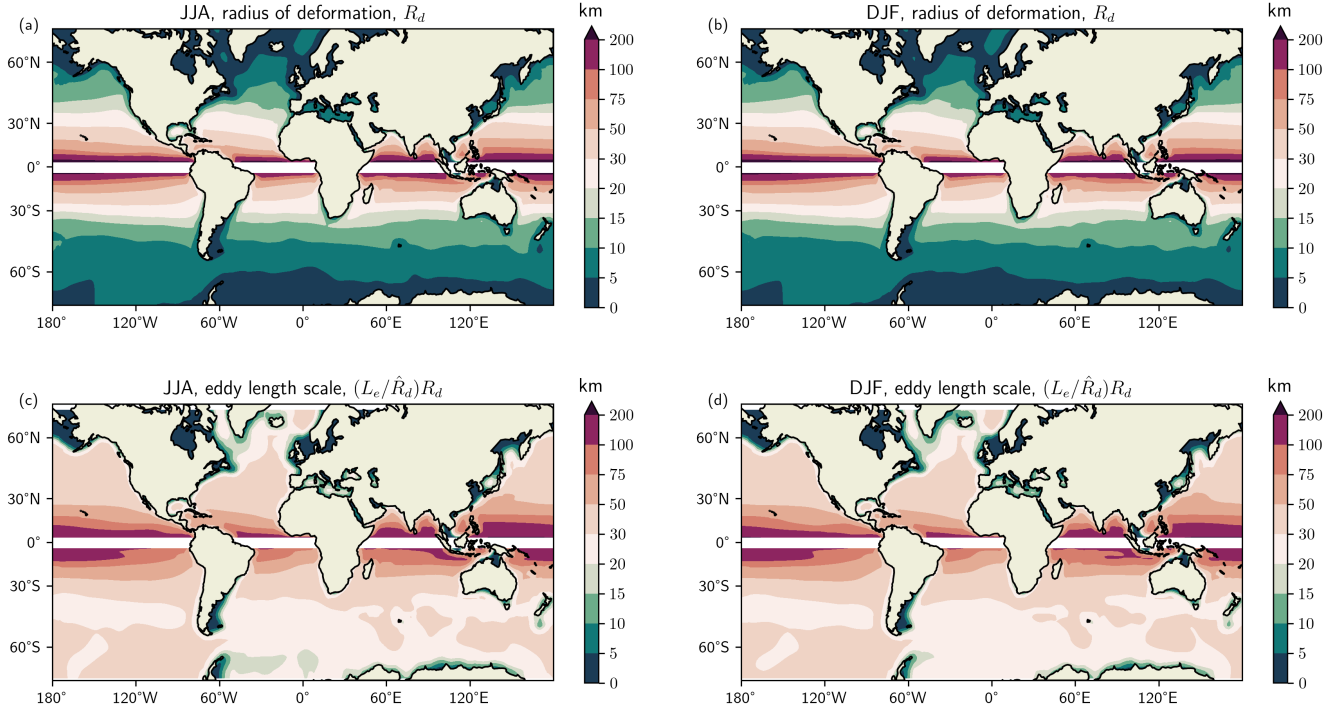
Figure 7. Global maps between the latitudes of 70°S and 70°N displaying the eddy length scale (in units km) for: left) JJA; and right) DJF. In a,b), first baroclinic Rossby radius of deformation, R_d, c,d) the eddy e-folding length scale, $(L_e/\hat{R}_d)R_d$. The R_d is calculated from World Ocean Atlas and NOAA datasets over 1981-2010 period, and $(L_e/\hat{R}_d)R_d$ is computed using data from Chelton et al. (2011). A latitude band between 5°S and 5°N has been masked out. The colourbar has uneven intervals, with spacing increasing with length scale.

suggested to be too high for this region, and our weaker Λ_{rel} from the Gulf Stream towards the interior here may hint at that being true. The Kuroshio Extension in the Northwest Pacific also displays values close to zero, but like the Gulf Stream, its values are overall much less pronounced when compared with those in the Southern Ocean. In the equatorial and tropic regions, $\log_{10}(\Lambda_{rel}/10^{-7}\ \text{s}^{-1})$ is mostly positive with contributions from wind speed and reduced gravity. Similarly to that in Fig. 7, the equator region has been masked due to the presence of the Coriolis parameter in the denominator of Λ_{rel} in (28). Comparing both seasons for each eddy length scale, the spatial pattern in $\log_{10}(\Lambda_{rel}/10^{-7}\ \text{s}^{-1})$ is similar, with only minor differences arising from changes in $|\boldsymbol{u}_a|$, μ, g', and R_d.

Figure 8c,d shows the dissipation rate that depends on the e-folding length scale, $(L_e/\hat{R}_d)R_d$. We see that $\log_{10}(\Lambda_{rel}/10^{-7}\ \text{s}^{-1})$ is largely negative, except over the equatorial region. Throughout the Southern Ocean and western boundaries, we find that Λ_{rel} is around a tenth to a quarter the size of $10^{-7}\ \text{s}^{-1}$. We also see that the ~~patterns are similar to those~~ pattern is similar to that seen in $\Lambda_{rel}(R_d)$ (Fig. 8a,b), ~~since~~ particularly across the North West Atlantic and Southern Ocean. This is clearly because the spatial pattern of the chosen eddy length scale (R_d or $(L_e/\hat{R}_d)R_d$) ~~does not vary, as~~ are similar, since $(L_e/\hat{R}_d)R_d$ depends on R_d.
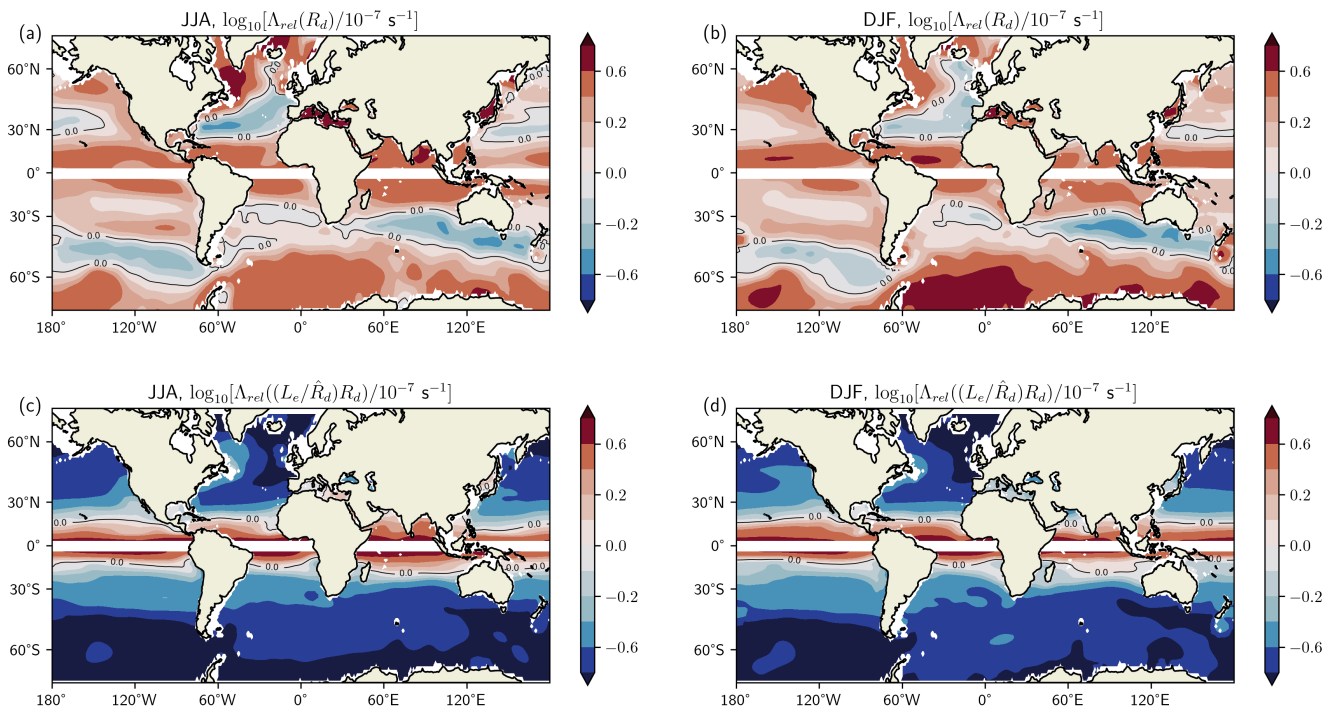
Figure 8. A global dissipation rate for relative wind stress damping, Λ_{rel} for: left) JJA; and right) DJF. In a,b) Λ_{rel} is a function of R_d, and c,d) Λ_{rel} is a function of $(L_e/\hat{R}_d)R_d$. The dissipation rate is normalised by a constant dissipation rate, 10^{-7} s^{-1} used in Mak et al. (2018). It is then shown on a $\log_{10}$ plot. The colourbar has uneven intervals, with smaller steps around zero to highlight when both dissipation rates are equivalent, or Λ_{rel} is marginally less than or greater than 10^{-7} s^{-1}. The thick contour line represents the point where $\Lambda_{rel} = 10^{-7}$ s^{-1}. A latitude band between 5°S and 5°N has been masked out.

430   Contrasting the two choices of eddy length scale is summarised using a density plot of $(\Lambda_{rel}/10^{-7}$ s$^{-1})\widehat{\text{lon}}$ in Fig. 9. Here, we have weighted $\Lambda_{rel}/10^{-7}$ s^{-1} with a normalised longitude (~~lon~~$\widehat{\text{lon}} = \text{lon}/\max(\text{lon})$), where the largest weight is at the lowest latitude. The density of dissipation rates depending on $(L_e/\hat{R}_d)R_d$ are skewed to the left and exhibit a narrow range centred around 0.2. The density of the dissipation rate depending on R_d is shifted to the right and displays a wider range of values centred close to 1. What Fig. 9 shows is that the dissipation rate due to relative wind stress may lie somewhere between 435 2×10^{-8} s^{-1} and 4×10^{-7} s^{-1}.

6   Summary and discussion

In this work we have presented a constrained eddy energy dissipation rate for a well-known and important mesoscale dissipation pathway, relative wind stress. Deriving this dissipation rate draws on our fundamental understanding of relative wind stress damping, vertical eddy structure, and eddy energy. The intention with this dissipation rate is for it to fit into an existing eddy
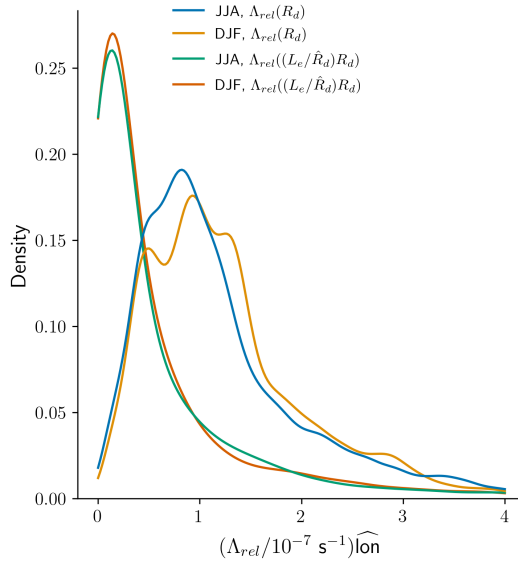
Figure 9. Kernel density estimation of $(\Lambda_{rel}/10^{-7}\text{ s}^{-1})\widehat{\text{lon}}$, where $\widehat{\text{lon}}$ is a normalised longitude. The four lines represent the dissipation rate Λ_{rel} depending on the chosen eddy length scale and season (DJF or JJA). Values over the equator band between 5°S and 5°N are not included here.

energy budget-based eddy parameterisation (e.g. GEOMETRIC), and offer improvements to the relatively unconstrained and spatially homogenous dissipation rate currently employed.

Before the proposition of a dissipation rate, an approximate expression for relative wind stress damping, termed P_{rel}, was found in Sec. 2.1. Several assumptions were made to help achieve this expression found in Eq. (11): mesoscale eddies are, on average, Gaussian in shape over the global ocean (Chelton et al., 2011); and the wind field is constant in strength and direction (Duhaut and Straub, 2006). Thereafter, P_{rel} is used to predict the decay of baroclinic eddy energy in a analytical two-layer model, which is described in Sect. 2.2. The analytical model is chosen to represent a mesoscale eddy with a first baroclinic mode structure, consistent with the first baroclinic mode containing a high portion of eddy energy. Then, comparing the evolution of eddy energy in the analytical model with a general circulation model shows that the expression for relative wind stress damping can approximate the decay of eddy energy well in each eddy type up to 150 days (Fig. 3). However, it is important to highlight that these results are dependent on our choice of model parameters. For example, while the numerical model diverges from the analytical around day 150, making changes to the eddy amplitude could affect the timescale of divergence. To quantify what these changes may lead to would require additional experiments. Nevertheless, we would still expect damping by ~~winds~~ relative wind stress to be the same across each model due to the matching of eddy amplitude.

The key component of this work lies in the proposed dissipation rate for eddy energy due to relative wind stress, outlined in Sect. 5. The dissipation rate Λ_{rel} culminates from the theory given in Sect. 2 and the verification of P_{rel} through the use of a general circulation model in Sect. 4. Deriving the dissipation rate Λ_{rel} in Eq. (26) is based on a simple two-layer analytical

model that exhibits a first baroclinic mode structure. This model is chosen because the eddy sea surface height reflects the movement of the first baroclinic mode, and can as such represent a large portion of eddy energy (Chelton et al., 1998). An analytical expression for total eddy energy E is then calculated from the two-layer theory. From this, we are able to construct an eddy energy dissipation rate due to relative wind stress, $\Lambda_{rel} = P_{rel}/E$. This dissipation rate is assumed to depend on available potential energy in the thermocline, and not kinetic energy. So whilst relative wind stress damps the surface geostrophic motion, the greater dynamical impact is for relative wind stress to relax the eddy thermocline displacement, and damp potential energy.

A global map of the dissipation rate is presented in Sect. 5 along with the terms that contribute to it. The eddy length scale is considered to be either the first baroclinic Rossby radius of deformation (R_d), acquired by solving a typical eigenvalue problem, or an e-folding length scale $\left((L_e/\hat{R}_d)R_d\right)$, computed using data from Chelton et al. (2011). The two eddy length scales help to form a range of values that Λ_{rel} could take. The dissipation rate Λ_{rel} is shown in Fig. 8 normalised by a constant dissipation rate 10^{-7} s^{-1} on a $\log_{10}$ plot. For R_d, we find that Λ_{rel} is greater than 10^{-7} s^{-1} across much of the ocean, with hotspots throughout the Southern Ocean, tropics, and equatorial regions. In the western boundary currents, Λ_{rel} is closer to 10^{-7} s^{-1}. For $(L_e/\hat{R}_d)R_d$, Λ_{rel} is less than 10^{-7} s^{-1} over most of the ocean except the equatorial region. However, Λ_{rel} still makes up to a quarter of 10^{-7} s^{-1} in regions like the Southern Ocean and western boundaries. Enhanced eddy energy dissipation in the Southern Ocean could impact heat and mass transport (Meijers et al., 2007; Stewart and Thompson, 2015), the exchange of heat and carbon at the air-sea interface (Villas Bôas et al., 2015; Pezzi et al., 2021), and Antarctic sea-ice cover (Munday et al., 2021). Seasonal variations are also present in the dissipation rate, particularly in eddy rich regions, and are consistent with changes in wind speed and stratification. High frequency wind events can also take place (Zhai et al., 2012), which may significantly modulate eddy energy dissipation in some regions. In addition to the interpretation of the dissipation in Fig. 8, validation of these values could be made in a further study through the computation of eddy available potential energy (von Storch et al., 2012) and use of a eddy detection method (Chelton et al., 2011) to quantify wind power input.

The dissipation rate is based on a simple energy budget derived from a two-layer analytical model, which by design neglects many phenomena that take place in the ocean, such as instabilities and wave dynamics. In the time evolution of total eddy energy (Fig. 3), the predicted and MITgcm results were shown to diverge around day 150 in each eddy type. Total eddy energy in MITgcm was found to undergo an exponential like decay for around 20 days, which corresponded with a change in eddy shape (Fig. 4). A foundation of the prediction method assumes that the baroclinic eddy remains circular, however, this is clearly not the case. The MITgcm eddy begins as a coherent structure, and then transitions into two smaller eddies. The splitting of a baroclinic eddy is due to baroclinic instability and leads to the formation of two barotropic eddies via barotropization (Ikeda, 1981; Dewar et al., 1999). This suggests that our predictive method could benefit from including an additional model that accounts for a smooth transition to the two smaller barotropic eddies. Indeed, the timescale for this transition could depend on a baroclinic mode timescale, and might even depend on eddy polarity. Whether accounting for this process in this prediction method is important for long climate timescales is something that could be investigated in a future body of work.

An alternative approach to the one taken in this paper might be to employ a different representation for the first baroclinic mode, and therefore analytical and numerical setups. In this work we followed the ideas of Wunsch (1997), where the first baroclinic mode is computed using a flat bottom and that horizontal bottom velocities are not zero. The choice of the two-layer

model and numerical setup is justified by the flat bottom first baroclinic mode. However, a further possibility could be surface modes (de La Lama et al., 2016). Surface modes ~~are computed using rough bathymetry and display horizontal bottom velocities that are zero~~ can be computed over variable topography and horizontal velocities at the bottom tend to be smaller than if a flat bottom is assumed. A analytical model that provides these surface modes could take the form of the two-layer quasi-geostrophic equations (Cushman-Roisin and Beckers, 2006), whilst a numerical setup may simply resemble an exponential decay from the surface to the bottom. Furthermore, surface modes may even provide a value for the Rossby radius of deformation that sits between our computed values of R_d and $(L_e/\hat{R}_d)R_d$ (LaCasce and Groeskamp, 2020). The nature of surface modes do then seem appealing. Yet, the idealised two-layer model we use in this study certainly comes with a number of benefits, not least its relatively simple analytical theory, which might not be the case in a quasi-geostrophic model.

This study presents a constrained eddy energy dissipation rate due to relative wind stress damping. Although relative wind stress is not the only mechanism associated with eddy energy dissipation, its focus in this study is grounded in the effects it has on ocean dynamics and ocean processes (Seo et al., 2016; Wu et al., 2017; Renault et al., 2019). A further advantage of this work is having a simple analytical expression for this dissipation rate that can be applied to ocean datasets. Being able to then illustrate the global variability in the eddy energy dissipation rate due to relative wind stress enables the discussion of possible implications this could have on wider climate processes. Areas of immediate future work should look to determine a reasonable approximation for eddy length scale and examine the impacts of this dissipation rate in a global ocean model. Furthermore, we hope the work here could provide the basis for similar studies looking to constrain an eddy energy dissipation rate, improving the energetics and flow in global ocean models.

Code and data availability. NCEP-NCAR Reanalysis 1 wind speed data provided by the NOAA PSL (NOAA PSL, https://psl.noaa.gov/data/gridded/data.ncep.reanalysis.html, last access: 10th November 2022). Temperature and salinity data is from World Ocean Atlas provided by NOAA NCEI (NOAA NCEI, https://www.ncei.noaa.gov/access/world-ocean-atlas-2018/, last access: 10th November 2022). The remaining data, including the computed dissipation rates, and code to reproduce the results in this work can be found at doi.org/10.5281/zenodo.8341660.

Author contributions. All authors contributed to the conception and design of this work. TW worked on the analytical derivations and its numerical solution, idealised model design, formal analysis, figure production, and writing - original and review. XZ provided supervision of the work, administered the project, assisted in solving the eigenvalue problem, and writing - review and editing. DM provided supervision of the work, assisted in the analytical work and MITgcm setup, and writing - review and editing. MJ provided supervision of the work, and writing - review and editing.

Competing interests. The authors declare that they have no conflict of interest.

Acknowledgements. This work was funded by the Natural Environment Research Council through the EnvEast Doctoral Training Partnership (Grant NE/L002582/1) and the European Union's Horizon 2020 research and innovation programme under grant agreement No. 101003536 (ESM2025–Earth System Models for the Future). The authors would also like to thank the Open Access Team at the University of Reading, for their assistance in organising the funding of this paper. TW thanks XZ, DM and MJ for their guidance and mentorship throughout this work. Further thanks goes to Julian Mak and an anonymous reviewer who have provided constructive feedback and thought provoking suggestions. The research presented in this paper was carried out on the High Performance Computing Cluster supported by the Research and Specialist Computing Support service at the University of East Anglia.

References

Arbic, B. K. and Flierl, G. R.: Baroclinically Unstable Geostrophic Turbulence in the Limits of Strong and Weak Bottom Ekman Friction: Application to Midocean Eddies, J. Phys. Oceanogr., 34, 2257–2273, https://doi.org/10.1175/1520-0485(2004)034<2257:BUGTIT>2.0.CO;2, 2004.

Bachman, S. D.: The GM+E Closure: A Framework for Coupling Backscatter with the Gent and McWilliams Parameterization, Ocean Model., 136, 85–106, https://doi.org/10.1016/j.ocemod.2019.02.006, 2019.

Barkan, R., Winters, K. B., and McWilliams, J. C.: Stimulated Imbalance and the Enhancement of Eddy Kinetic Energy Dissipation by Internal Waves, J. Phys. Oceanogr., 47, 181–198, https://doi.org/10.1175/JPO-D-16-0117.1, 2017.

Charney, J. G.: Geostrophic Turbulence, J. Atmospheric Sci., 28, 1087–1095, https://doi.org/10.1175/1520-0469(1971)028<1087:GT>2.0.CO;2, 1971.

Chelton, D. B., deSzoeke, R. A., Schlax, M. G., Naggar, K. E., and Siwertz, N.: Geographical Variability of the First Baroclinic Rossby Radius of Deformation, J. Phys. Oceanogr., 28, 433–460, https://doi.org/10.1175/1520-0485(1998)028<0433:GVOTFB>2.0.CO;2, 1998.

Chelton, D. B., Schlax, M. G., and Samelson, R. M.: Global Observations of Nonlinear Mesoscale Eddies, Prog. Oceanogr., 91, 167–216, https://doi.org/10.1016/j.pocean.2011.01.002, 2011.

Chen, R., Flierl, G. R., and Wunsch, C.: A Description of Local and Nonlocal Eddy–Mean Flow Interaction in a Global Eddy-Permitting State Estimate, J. Phys. Oceanogr., 44, 2336–2352, https://doi.org/10.1175/JPO-D-14-0009.1, 2014.

Cushman-Roisin, B. and Beckers, J.-M.: Introduction to Geophysical Fluid Dynamics, vol. 101, Academic Press, 2 edn., 2006.

Danabasoglu, G., McWilliams, J. C., and Gent, P. R.: The Role of Mesoscale Tracer Transports in the Global Ocean Circulation, Science, 264, 1123–1126, https://doi.org/10.1126/science.264.5162.1123, 1994.

de La Lama, M. S., LaCasce, J. H., and Fuhr, H. K.: The Vertical Structure of Ocean Eddies, Dynamics and Statistics of the Climate System, 1, dzw001, https://doi.org/10.1093/climsys/dzw001, 2016.

Dewar, W. K. and Flierl, G. R.: Some Effects of the Wind on Rings, J. Phys. Oceanogr., 17, 1653–1667, https://doi.org/10.1175/1520-0485(1987)017<1653:SEOTWO>2.0.CO;2, 1987.

Dewar, W. K., Killworth, P. D., and Blundell, J. R.: Primitive-Equation Instability of Wide Oceanic Rings. Part II: Numerical Studies of Ring Stability, J. Phys. Oceanogr., 29, 1744–1758, https://doi.org/10.1175/1520-0485(1999)029<1744:PEIOWO>2.0.CO;2, 1999.

Dove, L. A., Balwada, D., Thompson, A. F., and Gray, A. R.: Enhanced Ventilation in Energetic Regions of the Antarctic Circumpolar Current, Geophys. Res. Lett., 49, e2021GL097 574, https://doi.org/10.1029/2021GL097574, 2022.

Duhaut, T. H. A. and Straub, D. N.: Wind Stress Dependence on Ocean Surface Velocity: Implications for Mechanical Energy Input to Ocean Circulation, J. Phys. Oceanogr., 36, 202–211, https://doi.org/10.1175/JPO2842.1, 2006.

Eden, C. and Greatbatch, R. J.: Towards a Mesoscale Eddy Closure, Ocean Model., 20, 223–239, https://doi.org/10.1016/j.ocemod.2007.09.002, 2008.

Ferrari, R. and Wunsch, C.: Ocean Circulation Kinetic Energy: Reservoirs, Sources, and Sinks, Annu. Rev. Fluid Mech., 41, 253–282, https://doi.org/10.1146/annurev.fluid.40.111406.102139, 2009.

Ferreira, D., Marshall, J., and Heimbach, P.: Estimating Eddy Stresses by Fitting Dynamics to Observations Using a Residual-Mean Ocean Circulation Model and Its Adjoint, J. Phys. Oceanogr., 35, 1891–1910, https://doi.org/10.1175/JPO2785.1, 2005.

Flierl, G. R.: Models of Vertical Structure and the Calibration of Two-Layer Models, Dynam. Atmos. Oceans, 2, 341–381, https://doi.org/10.1016/0377-0265(78)90002-7, 1978.

Gaube, P., Chelton, D. B., Samelson, R. M., Schlax, M. G., and O'Neill, L. W.: Satellite Observations of Mesoscale Eddy-Induced Ekman Pumping, J. Phys. Oceanogr., 45, 104–132, https://doi.org/10.1175/JPO-D-14-0032.1, 2015.

Gent, P. R. and McWilliams, J. C.: Isopycnal Mixing in Ocean Circulation Models, J. Phys. Oceanogr., 20, 150–155, https://doi.org/10.1175/1520-0485(1990)020<0150:IMIOCM>2.0.CO;2, 1990.

Gent, P. R., Willebrand, J., McDougall, T. J., and McWilliams, J. C.: Parameterizing Eddy-Induced Tracer Transports in Ocean Circulation Models, J. Phys. Oceanogr., 25, 463–474, https://doi.org/10.1175/1520-0485(1995)025<0463:PEITTI>2.0.CO;2, 1995.

Gill, A. E., Green, J. S. A., and Simmons, A. J.: Energy Partition in the Large-Scale Ocean Circulation and the Production of Mid-Ocean Eddies, Deep Sea Research and Oceanographic Abstracts, 21, 499–528, https://doi.org/10.1016/0011-7471(74)90010-2, 1974.

Gordon, C., Cooper, C., Senior, C. A., Banks, H., Gregory, J. M., Johns, T. C., Mitchell, J. F. B., and Wood, R. A.: The Simulation of SST, Sea Ice Extents and Ocean Heat Transports in a Version of the Hadley Centre Coupled Model without Flux Adjustments, Clim. Dynam., 16, 147–168, https://doi.org/10.1007/s003820050010, 2000.

Graham, R. M., de Boer, A. M., Heywood, K. J., Chapman, M. R., and Stevens, D. P.: Southern Ocean Fronts: Controlled by Wind or Topography?, J. Geophys. Res. Oceans, 117, https://doi.org/10.1029/2012JC007887, 2012.

Griffies, S. M., Winton, M., Anderson, W. G., Benson, R., Delworth, T. L., Dufour, C. O., Dunne, J. P., Goddard, P., Morrison, A. K., Rosati, A., Wittenberg, A. T., Yin, J., and Zhang, R.: Impacts on Ocean Heat from Transient Mesoscale Eddies in a Hierarchy of Climate Models, J. Clim., 28, 952–977, https://doi.org/10.1175/JCLI-D-14-00353.1, 2015.

Hallberg, R. and Gnanadesikan, A.: The Role of Eddies in Determining the Structure and Response of the Wind-Driven Southern Hemisphere Overturning: Results from the Modeling Eddies in the Southern Ocean (MESO) Project, J. Phys. Oceanogr., 36, 2232–2252, https://doi.org/10.1175/JPO2980.1, 2006.

Hirst, A. C. and McDougall, T. J.: Deep-Water Properties and Surface Buoyancy Flux as Simulated by a Z-Coordinate Model Including Eddy-Induced Advection, J. Phys. Oceanogr., https://doi.org/10.1175/1520-0485(1996)026<1320:DWPASB>2.0.CO;2, 1996.

Holland, W. R.: The Role of Mesoscale Eddies in the General Circulation of the Ocean—Numerical Experiments Using a Wind-Driven Quasi-Geostrophic Model, J. Phys. Oceanogr., 8, 363–392, https://doi.org/10.1175/1520-0485(1978)008<0363:TROMEI>2.0.CO;2, 1978.

Holland, W. R. and Lin, L. B.: On the Generation of Mesoscale Eddies and Their Contribution to the OceanicGeneral Circulation. I. A Preliminary Numerical Experiment, J. Phys. Oceanogr., 5, 642–657, https://doi.org/10.1175/1520-0485(1975)005<0642:OTGOME>2.0.CO;2, 1975.

Huang, C. and Xu, Y.: Update on the Global Energy Dissipation Rate of Deep-Ocean Low-Frequency Flows by Bottom Boundary Layer, J. Phys. Oceanogr., 48, 1243–1255, https://doi.org/10.1175/JPO-D-16-0287.1, 2018.

Hughes, C. W. and Wilson, C.: Wind Work on the Geostrophic Ocean Circulation: An Observational Study of the Effect of Small Scales in the Wind Stress, J. Geophys. Res. Oceans, 113, https://doi.org/10.1029/2007JC004371, 2008.

Ikeda, M.: Instability and Splitting of Mesoscale Rings Using a Two-Layer Quasi-Geostrophic Model on an f-Plane, J. Phys. Oceanogr., 11, 987–998, https://doi.org/10.1175/1520-0485(1981)011<0987:IASOMR>2.0.CO;2, 1981.

Jansen, M. F., Adcroft, A., Khani, S., and Kong, H.: Toward an Energetically Consistent, Resolution Aware Parameterization of Ocean Mesoscale Eddies, J. Adv. Model. Earth Syst., 11, 2844–2860, https://doi.org/10.1029/2019MS001750, 2019.

Jullien, S., Masson, S., Oerder, V., Samson, G., Colas, F., and Renault, L.: Impact of Ocean–Atmosphere Current Feedback on Ocean Mesoscale Activity: Regional Variations and Sensitivity to Model Resolution, J. Clim., 33, 2585–2602, https://doi.org/10.1175/JCLI-D-19-0484.1, 2020.

Kalnay, E., Kanamitsu, M., Kistler, R., Collins, W., Deaven, D., Gandin, L., Iredell, M., Saha, S., White, G., Woollen, J., Zhu, Y., Chelliah, M., Ebisuzaki, W., Higgins, W., Janowiak, J., Mo, K. C., Ropelewski, C., Wang, J., Leetmaa, A., Reynolds, R., Jenne, R., and Joseph, D.: The NCEP/NCAR 40-Year Reanalysis Project, Bull. Am. Meteorol. Soc., 77, 437–472, https://doi.org/10.1175/1520-0477(1996)077<0437:TNYRP>2.0.CO;2, 1996.

605   Klinck, J.: MATLAB Function Dynmodes.m, GitHub [Code], 2009.

LaCasce, J. H.: The Prevalence of Oceanic Surface Modes, Geophys. Res. Lett., 44, 11,097–11,105, https://doi.org/10.1002/2017GL075430, 2017.

LaCasce, J. H. and Groeskamp, S.: Baroclinic Modes over Rough Bathymetry and the Surface Deformation Radius, J. Phys. Oceanogr., 50, 2835–2847, https://doi.org/10.1175/JPO-D-20-0055.1, 2020.

610   Large, W. G. and Pond, S.: Open Ocean Momentum Flux Measurements in Moderate to Strong Winds, J. Phys. Oceanogr., 11, 324–336, https://doi.org/10.1175/1520-0485(1981)011<0324:OOMFMI>2.0.CO;2, 1981.

Locarnini, R. A., Mishonov, A. V., Baranova, O. K., Boyer, T. P., Zweng, M. M., Garcia, H. E., Reagan, J. R., Seidov, D., Weathers, K., Paver, C. R., and Smolyar, I.: World Ocean Atlas 2018, Volume 1: Temperature. A. Mishonov, Technical Editor., NOAA Atlas NESDIS 81, p. 52pp, 2019.

615   Mahdinia, M., Hassanzadeh, P., Marcus, P. S., and Jiang, C.-H.: Stability of Three-Dimensional Gaussian Vortices in an Unbounded, Rotating, Vertically Stratified, Boussinesq Flow: Linear Analysis, J. Fluid Mech., 824, 97–134, https://doi.org/10.1017/jfm.2017.303, 2017.

Mak, J., Marshall, D. P., Maddison, J. R., and Bachman, S. D.: Emergent Eddy Saturation from an Energy Constrained Eddy Parameterisation, Ocean Model., 112, 125–138, https://doi.org/10.1016/j.ocemod.2017.02.007, 2017.

Mak, J., Maddison, J. R., Marshall, D. P., and Munday, D. R.: Implementation of a Geometrically Informed and Energetically Constrained
620   Mesoscale Eddy Parameterization in an Ocean Circulation Model, J. Phys. Oceanogr., 48, 2363–2382, https://doi.org/10.1175/JPO-D-18-0017.1, 2018.

Mak, J., Avdis, A., David, T., Lee, H. S., Na, Y., Wang, Y., and Yan, F. E.: On Constraining the Mesoscale Eddy Energy Dissipation Time-Scale, J. Adv. Model. Earth Syst., 14, e2022MS003 223, https://doi.org/10.1029/2022MS003223, 2022a.

Mak, J., Marshall, D. P., Madec, G., and Maddison, J. R.: Acute Sensitivity of Global Ocean Circulation and Heat Content to Eddy Energy
625   Dissipation Timescale, Geophys. Res. Lett., 49, e2021GL097 259, https://doi.org/10.1029/2021GL097259, 2022b.

Marshall, D. P., Maddison, J. R., and Berloff, P. S.: A Framework for Parameterizing Eddy Potential Vorticity Fluxes, J. Phys. Oceanogr., 42, 539–557, https://doi.org/10.1175/JPO-D-11-048.1, 2012.

Marshall, D. P., Ambaum, M. H. P., Maddison, J. R., Munday, D. R., and Novak, L.: Eddy Saturation and Frictional Control of the Antarctic Circumpolar Current, Geophys. Res. Lett., 44, 286–292, https://doi.org/10.1002/2016GL071702, 2017.

630   Marshall, J., Adcroft, A., Hill, C., Perelman, L., and Heisey, C.: A Finite-Volume, Incompressible Navier Stokes Model for Studies of the Ocean on Parallel Computers, J. Geophys. Res. Oceans, 102, 5753–5766, https://doi.org/10.1029/96JC02775, 1997a.

Marshall, J., Hill, C., Perelman, L., and Adcroft, A.: Hydrostatic, Quasi-Hydrostatic, and Nonhydrostatic Ocean Modeling, J. Geophys. Res. Oceans, 102, 5733–5752, https://doi.org/10.1029/96JC02776, 1997b.

McDougall, T. and Barker, P.: Getting Started with TEOS-10 and the Gibbs Seawater (GSW) Oceanographic Toolbox, Tech. rep., SCOR/I-
635   APSO WG127, 2011.

McGillicuddy, D. J., Robinson, A. R., Siegel, D. A., Jannasch, H. W., Johnson, R., Dickey, T. D., McNeil, J., Michaels, A. F., and Knap, A. H.: Influence of Mesoscale Eddies on New Production in the Sargasso Sea, Nature, 394, 263–266, https://doi.org/10.1038/28367, 1998.

Meijers, A. J., Bindoff, N. L., and Roberts, J. L.: On the Total, Mean, and Eddy Heat and Freshwater Transports in the Southern Hemisphere of a $\frac{1}{8}^{\circ} \times \frac{1}{8}^{\circ}$ Global Ocean Model, J. Phys. Oceanogr., 37, 277–295, https://doi.org/10.1175/JPO3012.1, 2007.

640 Mkhinini, N., Coimbra, A. L. S., Stegner, A., Arsouze, T., Taupier-Letage, I., and Béranger, K.: Long-Lived Mesoscale Eddies in the Eastern Mediterranean Sea: Analysis of 20 Years of AVISO Geostrophic Velocities, J. Geophys. Res. Oceans, 119, 8603–8626, https://doi.org/10.1002/2014JC010176, 2014.

Munday, D. R. and Zhai, X.: Sensitivity of Southern Ocean Circulation to Wind Stress Changes: Role of Relative Wind Stress, Ocean Model., 95, 15–24, https://doi.org/10.1016/j.ocemod.2015.08.004, 2015.

645 Munday, D. R., Johnson, H. L., and Marshall, D. P.: The Role of Ocean Gateways in the Dynamics and Sensitivity to Wind Stress of the Early Antarctic Circumpolar Current, Paleoceanography, 30, 284–302, https://doi.org/10.1002/2014PA002675, 2015.

Munday, D. R., Zhai, X., Harle, J., Coward, A. C., and Nurser, A. J. G.: Relative vs. Absolute Wind Stress in a Circumpolar Model of the Southern Ocean, Ocean Model., 168, 101 891, https://doi.org/10.1016/j.ocemod.2021.101891, 2021.

Pacanowski, R. C.: Effect of Equatorial Currents on Surface Stress, J. Phys. Oceanogr., 17, 833–838, https://doi.org/10.1175/1520-

650 0485(1987)017<0833:EOECOS>2.0.CO;2, 1987.

Pezzi, L. P., de Souza, R. B., Santini, M. F., Miller, A. J., Carvalho, J. T., Parise, C. K., Quadro, M. F., Rosa, E. B., Justino, F., Sutil, U. A., Cabrera, M. J., Babanin, A. V., Voermans, J., Nascimento, E. L., Alves, R. C. M., Munchow, G. B., and Rubert, J.: Oceanic Eddy-Induced Modifications to Air–Sea Heat and CO2 Fluxes in the Brazil-Malvinas Confluence, Sci Rep, 11, 10 648, https://doi.org/10.1038/s41598-021-89985-9, 2021.

655 Rai, S., Hecht, M., Maltrud, M., and Aluie, H.: Scale of Oceanic Eddy Killing by Wind from Global Satellite Observations, Sci. Adv., 7, eabf4920, https://doi.org/10.1126/sciadv.abf4920, 2021.

Renault, L., Molemaker, M. J., Gula, J., Masson, S., and McWilliams, J. C.: Control and Stabilization of the Gulf Stream by Oceanic Current Interaction with the Atmosphere, J. Phys. Oceanogr., 46, 3439–3453, https://doi.org/10.1175/JPO-D-16-0115.1, 2016a.

Renault, L., Molemaker, M. J., McWilliams, J. C., Shchepetkin, A. F., Lemarié, F., Chelton, D., Illig, S., and Hall, A.: Modulation of Wind

660 Work by Oceanic Current Interaction with the Atmosphere, J. Phys. Oceanogr., 46, 1685–1704, https://doi.org/10.1175/JPO-D-15-0232.1, 2016b.

Renault, L., Marchesiello, P., Masson, S., and McWilliams, J. C.: Remarkable Control of Western Boundary Currents by Eddy Killing, a Mechanical Air-Sea Coupling Process, Geophys. Res. Lett., 46, 2743–2751, https://doi.org/10.1029/2018GL081211, 2019.

Scott, R. B. and Arbic, B. K.: Spectral Energy Fluxes in Geostrophic Turbulence: Implications for Ocean Energetics, J. Phys. Oceanogr., 37,

665 673–688, https://doi.org/10.1175/JPO3027.1, 2007.

Seo, H., Miller, A. J., and Norris, J. R.: Eddy–Wind Interaction in the California Current System: Dynamics and Impacts, J. Phys. Oceanogr., 46, 439–459, https://doi.org/10.1175/JPO-D-15-0086.1, 2016.

Smith, K. S. and Vallis, G. K.: The Scales and Equilibration of Midocean Eddies: Freely Evolving Flow, J. Phys. Oceanogr., 31, 554–571, https://doi.org/10.1175/1520-0485(2001)031<0554:TSAEOM>2.0.CO;2, 2001.

670 Stewart, A. L. and Thompson, A. F.: Eddy-Mediated Transport of Warm Circumpolar Deep Water across the Antarctic Shelf Break, Geophys. Res. Lett., 42, 432–440, https://doi.org/10.1002/2014GL062281, 2015.

Tandon, A. and Garrett, C.: On a Recent Parameterization of Mesoscale Eddies, J. Phys. Oceanogr., 26, 406–411, https://doi.org/10.1175/1520-0485(1996)026<0406:OARPOM>2.0.CO;2, 1996.

Treguier, A. M., Held, I. M., and Larichev, V. D.: Parameterization of Quasigeostrophic Eddies in Primitive Equation Ocean Models, J. Phys.

675 Oceanogr., 27, 567–580, https://doi.org/10.1175/1520-0485(1997)027<0567:POQEIP>2.0.CO;2, 1997.

Vallis, G. K.: Atmospheric and Oceanic Fluid Dynamics: Fundamentals and Large-Scale Circulation, Cambridge University Press, Cambridge, 2 edn., https://doi.org/10.1017/9781107588417, 2017.

Villas Bôas, A. B., Sato, O. T., Chaigneau, A., and Castelão, G. P.: The Signature of Mesoscale Eddies on the Air-Sea Turbulent Heat Fluxes in the South Atlantic Ocean, Geophys. Res. Lett., 42, 1856–1862, https://doi.org/10.1002/2015GL063105, 2015.

680 Visbeck, M., Marshall, J., Haine, T., and Spall, M.: Specification of Eddy Transfer Coefficients in Coarse-Resolution Ocean Circulation Models, J. Phys. Oceanogr., 27, 381–402, https://doi.org/10.1175/1520-0485(1997)027<0381:SOETCI>2.0.CO;2, 1997.

von Storch, J.-S., Eden, C., Fast, I., Haak, H., Hernández-Deckers, D., Maier-Reimer, E., Marotzke, J., and Stammer, D.: An Estimate of the Lorenz Energy Cycle for the World Ocean Based on the STORM/NCEP Simulation, J. Phys. Oceanogr., 42, 2185–2205, https://doi.org/10.1175/JPO-D-12-079.1, 2012.

685 Wang, Y., Claus, M., Greatbatch, R. J., and Sheng, J.: Decomposition of the Mean Barotropic Transport in a High-Resolution Model of the North Atlantic Ocean, Geophys. Res. Lett., 44, 11,537–11,546, https://doi.org/10.1002/2017GL074825, 2017.

Wilder, T.: Mesoscale Ocean Eddy-Wind Interaction, Doctoral, University of East Anglia. School of Environmental Sciences, 2022.

Wilder, T., Zhai, X., Munday, D., and Joshi, M.: The Response of a Baroclinic Anticyclonic Eddy to Relative Wind Stress Forcing, J. Phys. Oceanogr., 52, 2129–2142, https://doi.org/10.1175/JPO-D-22-0044.1, 2022.

690 Wu, Y., Zhai, X., and Wang, Z.: Decadal-Mean Impact of Including Ocean Surface Currents in Bulk Formulas on Surface Air–Sea Fluxes and Ocean General Circulation, J. Climate, 30, 9511–9525, https://doi.org/10.1175/JCLI-D-17-0001.1, 2017.

Wunsch, C.: The Vertical Partition of Oceanic Horizontal Kinetic Energy, J. Phys. Oceanogr., 27, 1770–1794, https://doi.org/10.1175/1520-0485(1997)027<1770:TVPOOH>2.0.CO;2, 1997.

Wunsch, C. and Stammer, D.: SaTELlite Altimetry, the Marine Geoid, and the Oceanic General Circulation, Annu. Rev. Earth Planet. Sci., 695 26, 219–253, https://doi.org/10.1146/annurev.earth.26.1.219, 1998.

Xu, C., Shang, X.-D., and Huang, R. X.: Estimate of Eddy Energy Generation/Dissipation Rate in the World Ocean from Altimetry Data, Ocean Dynamics, 61, 525–541, https://doi.org/10.1007/s10236-011-0377-8, 2011.

Xu, C., Zhai, X., and Shang, X.-D.: Work Done by Atmospheric Winds on Mesoscale Ocean Eddies, Geophys. Res. Lett., 43, 12,174–12,180, https://doi.org/10.1002/2016GL071275, 2016.

700 Youngs, M. K., Thompson, A. F., Lazar, A., and Richards, K. J.: ACC Meanders, Energy Transfer, and Mixed Barotropic–Baroclinic Instability, J. Phys. Oceanogr., 47, 1291–1305, https://doi.org/10.1175/JPO-D-16-0160.1, 2017.

Zhai, X. and Greatbatch, R. J.: Surface Eddy Diffusivity for Heat in a Model of the Northwest Atlantic Ocean, Geophys. Res. Lett., 33, https://doi.org/10.1029/2006GL028712, 2006.

Zhai, X. and Greatbatch, R. J.: Wind Work in a Model of the Northwest Atlantic Ocean, Geophys. Res. Lett., 34, 705 https://doi.org/10.1029/2006GL028907, 2007.

Zhai, X. and Yang, Z.: Eddy-Induced Meridional Transport Variability at Ocean Western Boundary, Ocean Model., 171, 101 960, https://doi.org/10.1016/j.ocemod.2022.101960, 2022.

Zhai, X., Johnson, H. L., and Marshall, D. P.: Significant Sink of Ocean-Eddy Energy near Western Boundaries, Nature Geosci, 3, 608–612, https://doi.org/10.1038/ngeo943, 2010.

710 Zhai, X., Johnson, H. L., Marshall, D. P., and Wunsch, C.: On the Wind Power Input to the Ocean General Circulation, J. Phys. Oceanogr., 42, 1357–1365, https://doi.org/10.1175/JPO-D-12-09.1, 2012.

Zhang, Y. and Vallis, G. K.: Ocean Heat Uptake in Eddying and Non-Eddying Ocean Circulation Models in a Warming Climate, J. Phys. Oceanogr., 43, 2211–2229, https://doi.org/10.1175/JPO-D-12-078.1, 2013.

Zweng, M. M., Reagan, J. R., Seidov, D., Boyer, T. P., Locarnini, R. A., Garcia, H. E., Mishonov, A. V., Baranova, O. K., Weathers, K.,
715   Paver, C. R., and Smolyar, I.: World Ocean Atlas 2018, Volume 2: Salinity. A. Mishonov Technical Ed., NOAA Atlas NESDIS 82, p.
50pp, 2019.